Article

Sex-specific perturbations of neuronal development caused by mutations in the autism risk gene *DDX3X*

Adele Mossa[1,2,3,4,5], Lauren Dierdorff[1,2,3,4,5,10], Jeronimo Lukin[1,2,3,4,5,10], Marta Garcia-Forn[1,2,3,4,5], Wei Wang[6], Fatemeh Mamashli[7], Yeaji Park[1,2,3,4,5], Chiara Fiorenzani[1,2,3,4,5], Zeynep Akpinar[1,2,3,4,5,8], Janine Kamps[7], Jörg Tatzelt[7,9], Zhuhao Wu[6] & Silvia De Rubeis[1,2,3,4,5]✉

DDX3X is an X-linked RNA helicase that escapes X chromosome inactivation and is expressed at higher levels in female brains. Mutations in *DDX3X* are associated with intellectual disability (ID) and autism spectrum disorder (ASD) and are predominantly identified in females (DDX3X syndrome). Using cellular and mouse models, we show that *Ddx3x* mediates sexual dimorphisms in brain development at a molecular, cellular, and behavioral level. During cortical neuronal development, *Ddx3x* sustains a female-biased signature of enhanced ribosomal biogenesis and mRNA metabolism. Compared to male neurons, female neurons display larger nucleoli, higher expression of a set of ribosomal proteins, and a higher cytoplasm-to-nucleus ratio of ribosomal RNA. All these sex dimorphisms are obliterated by *Ddx3x* loss. *Ddx3x* regulates dendritic arborization complexity in a sex- and dose-dependent manner in both female and male neurons. *Ddx3x* modulates the development of dendritic spines but only in female neurons. Further, ablating *Ddx3x* conditionally in forebrain neurons is sufficient to yield sex-specific changes in developmental outcomes and motor function. Together, these findings pose *Ddx3x* as a mediator of sexual differentiation during neurodevelopment and open new avenues to understand sex differences in health and disease.

Genetic variation in the X-linked gene *DDX3X* is a leading cause of intellectual disability (ID) and autism spectrum disorder (ASD)[1–6] (DDX3X syndrome). Over 95% of individuals with *DDX3X* mutations are females, and they have de novo loss-of-function mutations leading to haploinsufficiency or missense mutations[2,3,5,7]. The few identified males have missense variants typically inherited from apparently asymptomatic mothers and thought to act as hypomorphic alleles[2,3,5,8]. Given that ASD and ID are disproportionally diagnosed and studied in males[9], DDX3X syndrome provides a unique window into sex differences in neurodevelopment.

[1]Seaver Autism Center for Research and Treatment, Icahn School of Medicine at Mount Sinai, New York, NY 10029, USA. [2]Department of Psychiatry, Icahn School of Medicine at Mount Sinai, New York, NY 10029, USA. [3]The Mindich Child Health and Development Institute, Icahn School of Medicine at Mount Sinai, New York, NY 10029, USA. [4]Friedman Brain Institute, Icahn School of Medicine at Mount Sinai, New York, NY 10029, USA. [5]Alper Center for Neural Development and Regeneration Friedman Brain Institute, Icahn School of Medicine at Mount Sinai, New York, NY 10029, USA. [6]Appel Alzheimer's Disease Research Institute, Feil Family Brain and Mind Research Institute, Weill Cornell Medicine, New York NY10021, USA. [7]Department Biochemistry of Neurodegenerative Diseases, Institute of Biochemistry and Pathobiochemistry, Ruhr University Bochum, Bochum, Germany. [8]Department of Biology, New York University, College of Arts and Science, New York, NY 10003, USA. [9]Cluster of Excellence RESOLV, Bochum, Germany. [10]These authors contributed equally: Lauren Dierdorff, Jeronimo Lukin. ✉e-mail: silvia.derubeis@mssm.edu

DDX3X encodes an ATP-dependent DEAD-box RNA helicase with broad functions in RNA metabolism[3,10–14], including regulating mRNA translation[10,11] and RNA-containing condensates and granules via liquid-liquid phase separation (LLPS)[15–19]. Complex mechanisms of mRNA translation accompany and shape brain development[20–23]. The functions of *DDX3X* in the brain are only beginning to emerge[3,12,24,25]. While *Ddx3x* null mice die *in utero*[24,26], *Ddx3x* haploinsufficient females have delays in meeting postnatal milestones, followed by adult behavioral and neurological deficits[24]. Evidence in this and other mouse models indicates that *Ddx3x* is indispensable for the development of the hindbrain[25] and the forebrain[3,12,24]. The neocortex is particularly vulnerable, as shown by the congenital brain malformations often diagnosed in individuals with DDX3X syndrome[2,3,5], and the experimental evidence showing that the birth[3,12] and laminar subtype specification[24] of cortical glutamatergic neurons require *Ddx3x*. In addition to these functions ingrained in prenatal development, prior evidence suggest that *Ddx3x* also regulates neuronal morphogenesis[27], which might further alter the integration of cortical glutamatergic neurons into local circuitries.

DDX3X escapes X chromosome inactivation and is expressed from both alleles in women[28–30] and female mice[24,31], including in the brain. Despite only a few ancestral genes having survived on the Y chromosome, *DDX3X* has retained a Y homologous gene (*DDX3Y*)[32–34]. Hence, *DDX3X* belongs to a class of X-linked genes with unique potential to drive sexual differentiation, through unbalanced expression and/or divergent functions of the Y homologue[33,35]. However, the interplay between *DDX3X* and *DDX3Y* remains poorly understood. In brain-conditional mouse models, *Ddx3x* null females have more pronounced brain cytoarchitecture anomalies than *Ddx3x* null males[12,25], which also show upregulated *Ddx3y* mRNA[12,25], suggesting mechanisms of compensation. However, *DDX3X* ablation in males is incompatible with life in humans and mice[5,24,26]. Also, *DDX3Y* deletions cause subfertility/infertility[36–38], not brain disorders, in line with the evolution of testis-restricting regulatory regions in this gene in primates[39].

DDX3X lies at the intersection of X chromosome biology, sexual differentiation, and risk for ID/ASD, and yet no studies have examined the differential effect of *Ddx3x* loss in female and male brains. Here, we address this gap by examining the influence of sex, *Ddx3x* gene dosage, and their interaction on neuronal development and behavioral outcomes translationally relevant for *DDX3X* mutations associated with ID and ASD. We show that *Ddx3x* mediates sexual dimorphisms during brain development, and that *Ddx3x* perturbations alter the development and function of cortical glutamatergic neurons in a sex-specific manner.

Results

Ddx3x defines the complexity of dendritic arborization in a dosage- and sex-dependent manner

To investigate the influence of sex and *Ddx3x* allelic dosage on neuronal development, we crossed *Ddx3x*[+/flox] females[24] with wild-type males (*Ddx3x*[+/y]) to obtain embryos of four genotypes: control females (*Ddx3x*^{+/+}), floxed heterozygous females (*Ddx3x*[+/flox]), control males (*Ddx3x*[+/y]), and floxed males (*Ddx3x*[flox/y]). By crossing *Ddx3x*[+/flox] females with *Ddx3x*[flox/y] males, we also obtained floxed homozygous females (*Ddx3x*[flox/flox]). Cortical neurons were isolated from embryos at embryonic (E) day 15 and transfected with a bicistronic construct carrying mCherry and CRE (pAAV-Ef1a-mCherry-IRES-Cre) at plating (day in vitro 0, DIV0) (Fig. 1A). Neurons were then cultured for 9 days, fixed, and imaged (Fig. 1A, B). As intended, this genetic manipulation resulted in sparsely labeled mCherry[+] control female neurons (*Ddx3x*^{+/+}), haploinsufficient female neurons (*Ddx3x*^{+/-}), null female neurons (*Ddx3x*^{-/-}), control male neurons (*Ddx3x*[+/y]), and null male neurons (*Ddx3x*[-/y]) (Fig. 1A–C).

In line with previous data that siRNA-mediated *Ddx3x* knockdown alters neurite outgrowth[27], *Ddx3x* deficiency reduced dendritic complexity: *Ddx3x*^{+/-}, *Ddx3x*^{-/-}, and *Ddx3x*[-/y] neurons had simplified dendritic arborizations (Fig. 1B–D–H) and reduced length of the overall dendritic arbor (Fig. 1I). These cellular deficits were both dosage- and sex-dependent. Female *Ddx3x*^{+/-} and *Ddx3x*^{-/-} neurons differed, indicating a gene dosage effect (Fig. 1D, Fig. 1F–I). Female *Ddx3x*^{+/-} and male *Ddx3x*[+/y] neurons had monoallelic *Ddx3x* expression and yet were dissimilar (Fig. 1D–G–I). Female *Ddx3x*^{-/-} and male *Ddx3x*[-/y] null neurons showed no overt differences in their dendritic arborization (Fig. 1D), but *Ddx3x*^{-/-} neurons had significantly less secondary and tertiary dendrites than *Ddx3x*[-/y] neurons (Fig. 1F, G).

To corroborate these findings in vivo, we took advantage of our *Sox2-Ddx3x* mouse model[24] and contrasted the dendritic morphology of cortical neurons from adult *Sox2-Ddx3x*^{+/-} and *Sox2-Ddx3x*^{+/+} brains. To this end, layer V pyramidal neurons were in vivo labeled by injecting retrograde adeno-associated viral particles (AAV) carrying GFP (rAVV-CAG-GFP) in the pontine reticular nucleus and performing brain tissue clearing and light-sheet microscopy three weeks post-surgery (see Methods). We prioritized this cortical subtype based on evidence of alterations of layer V neurons and motor deficits in *Sox2-Ddx3x*^{+/-} mice[24] and clinical observations of pontine hypoplasia in individuals with *DDX3X* mutations[3,40]. Retrograde viral tracing resulted in robust labeling of both controlateral and ipsilateral pyramidal neurons (Fig. 2A). Using Sholl analysis and focusing on neurons whose somata reside in the motor cortex, we found not overt genotype-driven changes in the overall dendritic arborization, but the *Sox2-Ddx3x*^{+/-} neurons had significantly fewer intersections at 600-700 μm from the soma (Fig. 2A, B). We also quantified the length of the proximal apical dendrite and the remaining dendritic tract that covers the distal apical dendrite and the terminal tuft (see Methods). We found that *Sox2-Ddx3x*^{+/-} neurons had longer proximal apical dendrite at the expense of the distal apical dendrite and tuft (Fig. 2C, D). Further, *Sox2-Ddx3x*^{+/-} neurons had simpler terminal tufts (Fig. 2E, F).

In sum, *Ddx3x* is indispensable for the development of proper dendritic arborization in a cell-autonomous manner in both female and male neurons, and this function depends on dosage and sex. The endogenous *Ddx3y* gene is unable to fully compensate for *Ddx3x* function in neuronal morphogenesis. Further, *Ddx3x* haploinsufficiency alters the dendritic arborization of corticopontine neurons residing in the motor cortex, with the greatest impact on processes extending to the upper layers, plausibly perturbing local circuitries.

Ddx3x regulates the development of dendritic spines in a sex-dependent manner

Following the previous reasoning, we sought to discriminate the effect of sex and *Ddx3x* dosage on the formation and maturation of dendritic spines. We adopted the same Cre-recombination strategy described above. To isolate the discrete function of *Ddx3x* in this process, sparse transfections were performed at DIV9 and neurons examined at DIV14 (Fig. 3A, B). This way, dendritogenesis proceeded unperturbed until the onset of synaptogenesis, and thus synaptic phenotypes were not confounded by earlier defects in dendritic development. 10 μm long segments at least 30 μm distant from the soma were then examined in DIV14 mCherry[+] *Ddx3x*^{+/+}, *Ddx3x*^{+/-}, *Ddx3x*^{-/-}, *Ddx3x*[+/y], or *Ddx3x*[-/y] neurons (Fig. 3A). The dendritic segments were examined across primary, secondary, and tertiary dendrites and in both thin and thick dendrites (Fig. S1).

Quantifications of dendritic density revealed that intact *Ddx3x* expression is indispensable for spines formation in females but not in males: *Ddx3x*^{-/-}, but not *Ddx3x*^{+/-} or *Ddx3x*[-/y] neurons, had more dendritic spines than control neurons (Fig. 3B, C). When measuring spine density as a function of distance from the soma, we noted that the increased number of spines in *Ddx3x*^{-/-} neurons was most prominent at 60-70 μm from the soma (Fig. 3D). Consistently, when assessing the spine density by dendrite hierarchy or diameter, we observed that the overexuberant
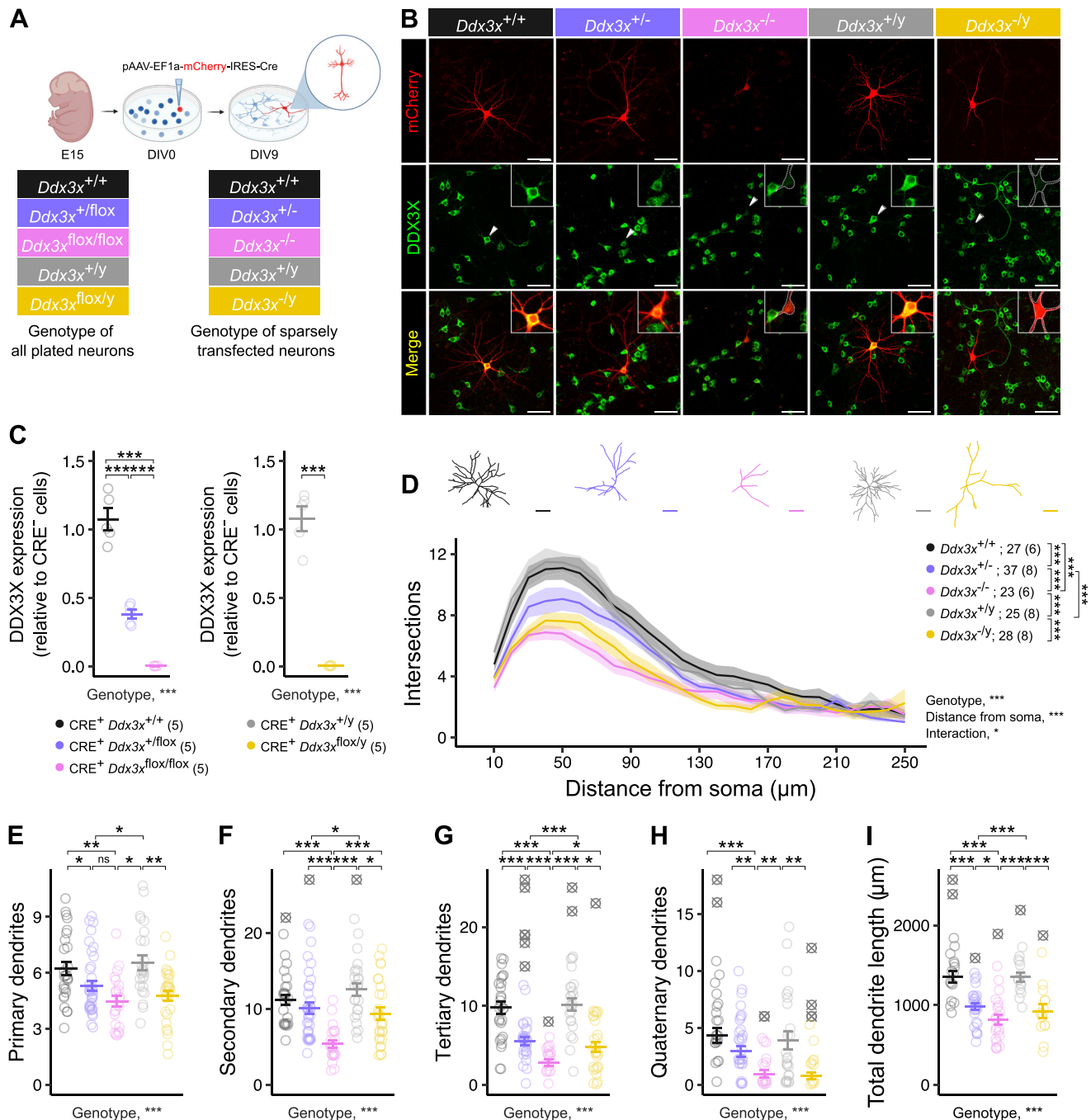
Fig. 1 | *Ddx3x* regulates dendritogenesis. A Experimental design. Cortical neurons are isolated from *Ddx3x*^{+/+}, *Ddx3x*[+/flox], *Ddx3x*[flox/flox], *Ddx3x*[+/y] or *Ddx3x*[flox/y] E15 embryos. The day of plating (DIV0), neurons are transfected with a construct carrying mCherry and CRE, resulting in sparsely labeled control female neurons (*Ddx3x*^{+/+}, black), haploinsufficient female neurons (*Ddx3x*^{+/-}, purple), null female neurons (*Ddx3x*^{-/-}, pink), control male neurons (*Ddx3x*[+/y], gray), or null male neurons (*Ddx3x*[-/y], yellow). Analyses are performed at DIV9. Created in BioRender[103]. **B–C** Validation of the *Ddx3x* manipulations in neuronal cultures. **B** Confocal images of DIV9 cortical neurons immunostained for mCherry (red) and DDX3X (green). Scale bar, 50 μm. **C** DDX3X expression in DIV9 CRE⁺mCherry⁺ neurons from *Ddx3x*^{+/+}, *Ddx3x*[+/flox], *Ddx3x*[flox/flox], *Ddx3x*[+/y], or *Ddx3x*[flox/y] embryos sparsely transfected at DIV0 (as in **B**), compared to neighboring untransfected neurons (CRE⁻mCherry⁻) within the same coverslip. The expression is shown as relative to CRE⁻mCherry⁻ cells, separately for female (left panel) and male (right panel) neurons. **D** Loss of *Ddx3x* causes a simplified dendritic arbor. The plot

shows the number of branching points as a function of the distance from the soma in DIV9 neurons across the five genotypes described in **A** and shown in **B**. Representative traces are shown on top of the plot. Scale bar, 50 μm. **E–H** Loss of *Ddx3x* causes a reduction in the number of dendrites. The plot shows the number of primary (**E**), secondary (**F**), tertiary (**G**) and quaternary dendrites (**H**) of DIV9 cortical neurons across five genotypes described in **A**. **I** Loss of *Ddx3x* reduces dendritic length. The plot shows the total lengths of dendrites of DIV9 cortical neurons across five genotypes described in **A**. Statistics: Panels **C** and **I**, One-way ANOVA, followed by Student's t test with Benjamini-Hochberg correction; Panel **D**, Repeated measure ANOVA, followed by Tukey test with Benjamini-Hochberg correction; Panel **E–H**, Kruskal-Wallis test, followed by Wilcoxon test with Benjamini-Hochberg correction. In all panels, data were collected blind to genotype and sex; *n* is shown in legend as number of neurons (and number of embryos); mean ± SEM; outliers (shown as ⊗), *P-value < 0.05, **P-value < 0.01, ***P-value < 0.001. Source data are provided as a Source Data file.
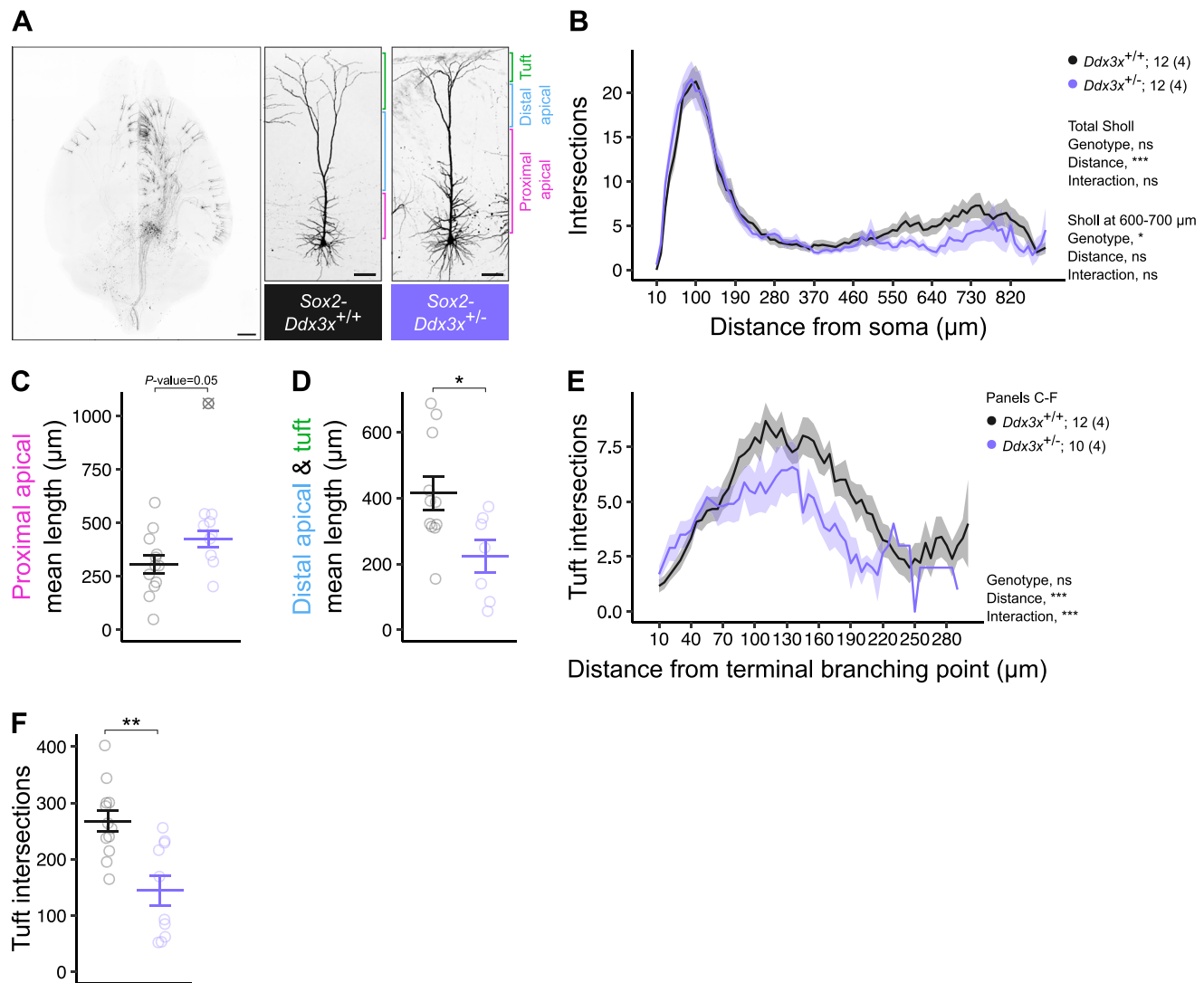
Fig. 2 | Corticopontine neurons from *Ddx3x* haploinsufficient mice have simplified dendritic arborizations. A In vivo labeled corticopontine neurons in control and *Ddx3x* haploinsufficient female mice. Left, horizontal 3D view of an iDISCO-cleared brain after in vivo retrograde labeling of corticopontine neurons. Scale bar, 1 mm. Right, representative GFP⁺ corticopontine neurons from *Sox2-Ddx3x*⁺/⁺ (black) or *Sox2-Ddx3x*⁺/⁻ (purple) brains. Scale bar, 100 μm. **B** *Ddx3x* haploinsufficiency affects the complexity of the distal apical dendrite. The plot shows the number of branching points as a function of the distance from the soma in GFP⁺ corticopontine neurons from *Sox2-Ddx3x*⁺/⁺ or *Sox2-Ddx3x*⁺/⁻ brains. **C** *Ddx3x* haploinsufficient neurons tend to have longer proximal apical dendrites. The plot shows the length of proximal apical dendrites in GFP⁺ corticopontine neurons from *Sox2-Ddx3x*⁺/⁺ or *Sox2-Ddx3x*⁺/⁻ brains. **D** *Ddx3x* haploinsufficient neurons have

shorter dendritic tracts covering the distal apical dendrites and the tuft. The plot shows the length of the dendritic tracts covering the distal apical dendrites and the tuft in GFP⁺ corticopontine neurons from *Sox2-Ddx3x*⁺/⁺ or *Sox2-Ddx3x*⁺/⁻ brains. **E, F** *Ddx3x* haploinsufficient neurons have simplified terminal tufts, as shown by the number of tuft intersections as a distance from the terminal branching point where the distal apical arborizes into the tuft (**E**) and the total number of intersections in the tuft (**F**) in GFP⁺ corticopontine neurons from *Sox2-Ddx3x*⁺/⁺ or *Sox2-Ddx3x*⁺/⁻ brains. Statistics: Panels **B** and **E**, repeated measure ANOVA; Panels **C**, **D**, and **F**, Student's t test. In all panels, data were collected blind to genotype and sex; *n* is shown in legend as number of neurons (and number of mice); mean ± SEM; outliers shown as ⊗; *P-value < 0.05, ***P-value < 0.001. Source data are provided as a Source Data file.

dendritic spines in *Ddx3x*⁻/⁻ neurons clustered to secondary and/or thin dendrites (Fig. S2).

To examine morphological characteristics, we measured the neck length and head width of individual dendritic spines. *Ddx3x*⁺/⁻ female neurons displayed increased neck length (Fig. 3F, G) and increased head width (Fig. 3H, I), when compared to *Ddx3x*⁺/⁺ or *Ddx3x*⁻/⁻ female neurons. Using the neck length and head width measures, we then classified dendritic spines into six morphological types: branched, mushroom, stubby, thin, long thin, and filopodia (Fig. 3E) (see Methods). When considering spines cumulatively, only *Ddx3x*⁺/⁻ female neurons had a distinct profile, with a surplus of mushroom-like and long thin spines at the expense of thin spines (Fig. 3E). We note that these data are in contrast with prior observations of reduced spine

density, excess of mushroom-like spines, and increase of filopodia after acute knockdown of *Ddx3x*, again without considering the variables of sex and allelic dosage[27].

Our data indicate that *Ddx3x* influences the development of dendritic spines in a cell-autonomous manner. This regulation is female-specific, as *Ddx3x* null male neurons are unaffected. The effect of dosage in female neurons is complex, as haploinsufficiency affects spines morphology but not density, and complete loss affects density but not morphology. These observations suggest that *Ddx3x* is required for both the formation and the maturation of dendritic spines: *Ddx3x* monoallelic expression is sufficient to repress excessive spines formation at an early phase and/or facilitate pruning at a later phase, but biallelic expression is required throughout spine maturation.
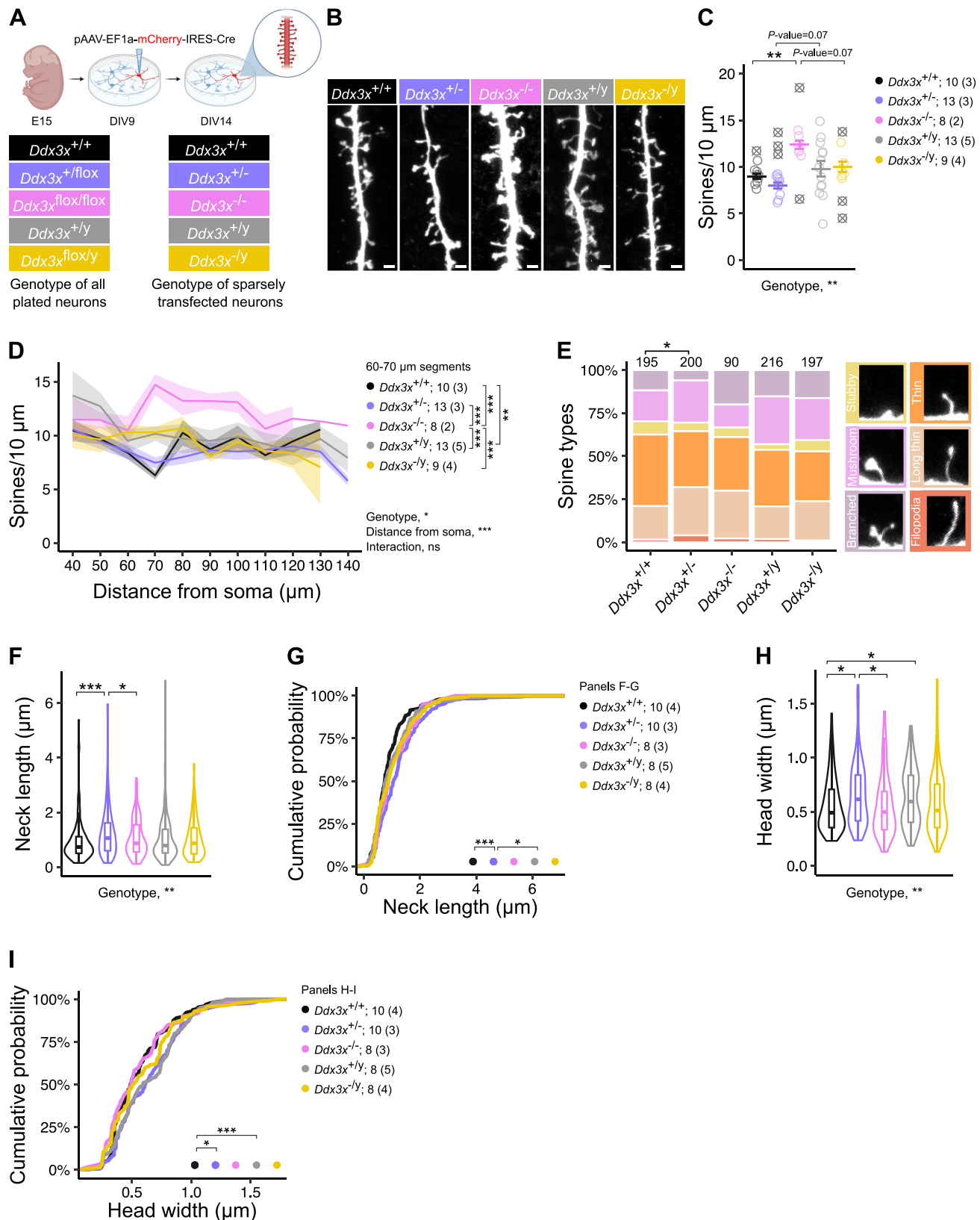
Ddx3x controls the female-biased expression of ribosomal proteins and mRNA translation regulators

We next investigated the molecular changes that accompany the cellular phenotypes resulting from *Ddx3x* mutations. To this end, we first transduced DIV0 cortical neurons from *Ddx3x*$^{+/+}$, *Ddx3x*$^{+/flox}$, *Ddx3x*$^{+/y}$ or *Ddx3x*$^{flox/y}$ embryos with AAV8-Ef1a-mCherry-IRES-Cre viral particles

(Fig. 4A). With this strategy, we obtained homogenous populations of *Ddx3x*$^{+/-}$ and *Ddx3x*$^{-/y}$ neurons, and their respective controls (Fig. 4A). We then performed label-free quantitative proteomics at DIV9, restricting analyses to proteins identified with at least two unique peptides (see Methods), and proceeded to identify up- and down-regulated proteins (indicated in the figure and below with their gene names, Fig. 4B–D).

Fig. 3 | *Ddx3x* regulates the formation and development of dendritic spines.
A Experimental design. Cortical neurons are isolated from *Ddx3x*^+/+^, *Ddx3x*^+/flox^,
Ddx3x^flox/flox^, *Ddx3x*^+/y^, or *Ddx3x*^flox/y^ E15 embryos. At DIV9, neurons are transfected
with the construct carrying mCherry and CRE, resulting in sparsely labeled *Ddx3x*^+/+^
(black), *Ddx3x*^+/-^ (purple), *Ddx3x*^-/-^ (pink), *Ddx3x*^+/y^ (gray), or *Ddx3x*^-/y^ (yellow) neu-
rons. Analyses are performed at DIV14. Created in BioRender[103]. **B** *Ddx3x* dosage
influences dendritic spine density. Confocal images of 10 μm dendritic segments
50 μm distant from the soma, showing mCherry-expressing dendritic shafts and
spines. Scale bar, 1 μm. **C** *Ddx3x* loss in female (but not male) neurons alters spine
density. The plot shows the number of dendritic spines in 10 μm. **D** Dendritic
density varies as a function of the distance from the soma. The plot shows the
number of dendritic spines in 10 μm as a function of distance from soma (values on
the X axis represent the upper boundary of the segment, e.g., 50 μm marks the 40-
50 μm segment). **E** *Ddx3x* haploinsufficiency alters the balance of spine subtypes.

The plot shows the proportion of dendritic spines across the six spine subtypes,
defined as indicated in the Methods section (*n* spines above each bar). **F, G** *Ddx3x*
haploinsufficiency results in increased spine neck length, as shown by the average
spine neck length (**F**) and the empirical cumulative distribution function of the
spine neck length measures (**G**). **H, I** *Ddx3x* haploinsufficiency results in increased
spine head width, as in **F, G** but for the spine head width. Statistics: Panel **C**, one-way
ANOVA, followed by Student's t test with Benjamini-Hochberg correction; Panel
D, repeated measure ANOVA, followed by Tukey test with Benjamini-Hochberg
correction at 60-70 μm segments. Panel **E**, Chi-square test. Panels **F** and **H**, Kruskal-
Wallis test, followed by Wilcoxon test with Benjamini-Hochberg correction. Panel
G and **I**, Kolmogorov–Smirnov test. In all panels, data were collected blind to
genotype and sex; *n* is shown in legend as number of neurons (and number of
embryos); mean ± SEM; outliers shown as ⊗; *P-value < 0.05, **P-value < 0.01,
***P-value < 0.001. Source data are provided as a Source Data file.

When comparing *Ddx3x*^+/+^ and *Ddx3x*^+/y^ genotypes, we found 193
dysregulated proteins (Supplementary Data 1A), specifically 114 pro-
teins with higher expression in female neurons than male neurons, and
79 proteins with the opposite sex bias in expression (Fig. 4B). *Ddx3x*
was one of the most differentially expressed proteins based on sex
(Fig. 4B, Supplementary Data 1A), in agreement with our prior data[24]
and human data (Fig. S3A). Interestingly, the only other X-linked pro-
tein detected, *Ubl4a*, also showed higher expression in female neu-
rons, suggesting that this gene might escape X chromosome
inactivation in murine neurons. However, no sex bias in expression is
seen for *UBL4A* in human tissues[29] (Fig. S3A). Also, the female-biased
expression for 4 genes in addition to *Ddx3x* (*Tufm, Scfd2, Lrpprc*, and
Eif3i) is conserved in the human cortex, as shown by bulk tran-
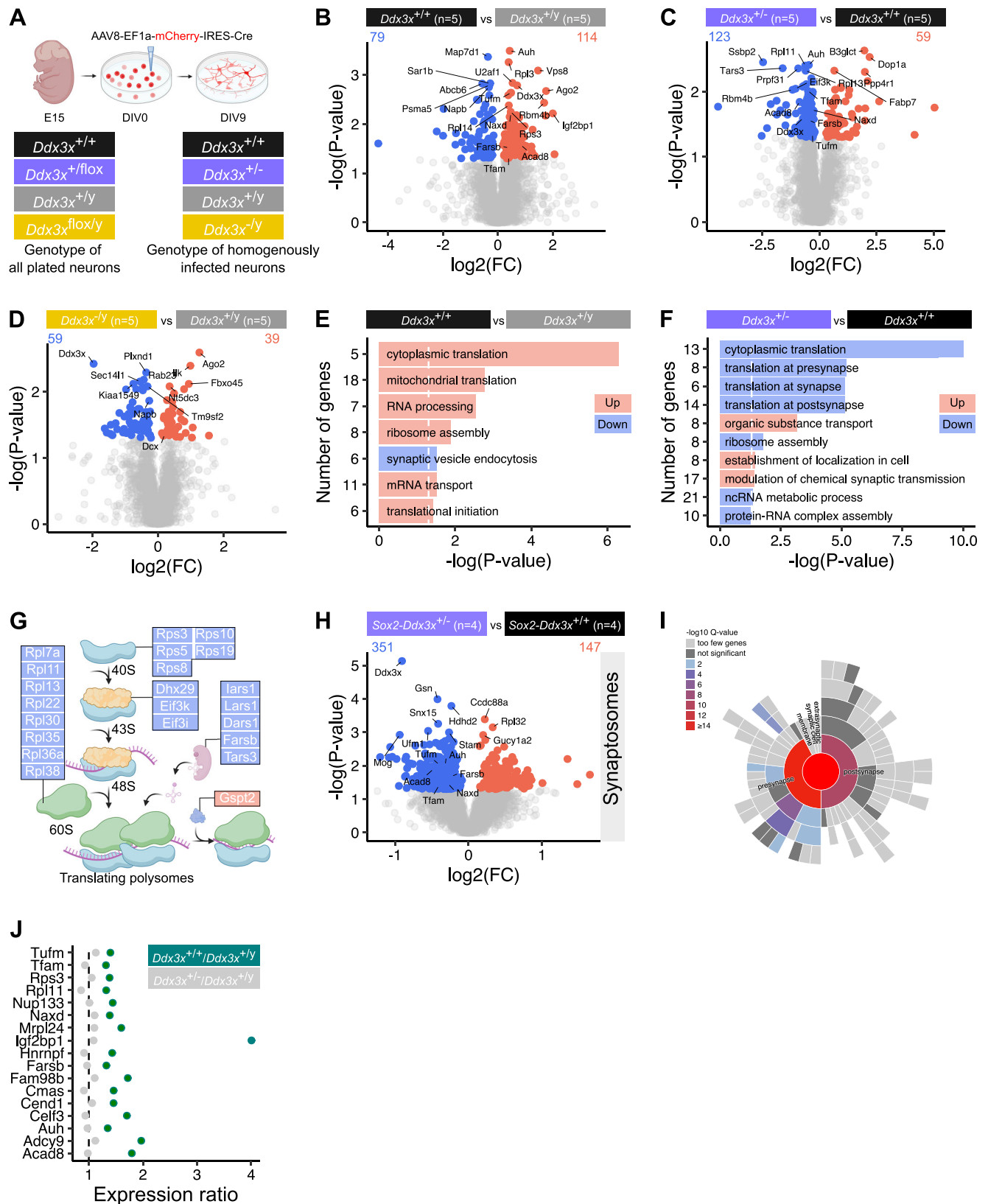scriptomic data[30] (Fig. S3B) (see Supplemental Note).

When comparing *Ddx3x*^+/-^ and *Ddx3x*^+/+^ genotypes, we found 182
dysregulated proteins (Supplementary Data 1B), specifically 59 up-
regulated and 123 down-regulated proteins (including *Ddx3x*) (Fig. 4C).
When comparing *Ddx3x*^-/y^ and *Ddx3x*^+/y^ genotypes, we found 98 dys-
regulated proteins (Supplementary Data 1C), specifically 39 up-
regulated and 59 down-regulated proteins (including *Ddx3x*)
(Fig. 4D). Previous analyses have detected *Ddx3y* mRNA in the brain[12,25].
However, since *DDX3Y* has been shown to undergo post-
transcriptional restriction in male germ cells[39,41], we analyzed our
proteomics data in search of DDX3Y-specific peptides in male neurons.
We identified a DDX3Y-specific peptide (KPILVATAVAAR in DDX3Y,
Uniprot #Q62095; SPILVATAVAAR in DDX3X, Uniprot #Q62167)
exclusively in the *Ddx3x*^-/y^ dataset. We also detected DDX3Y in *Ddx3x*^-/y^
cultures by Western blot (Fig. S4A). These data corroborate the
expression of DDX3Y, albeit at low levels, in male neurons after abla-
tion of *Ddx3x*.

We then interrogated biological processes annotated in Gene
Ontology (GO) with the datasets of 193 (Fig. 4B), 182 (Fig. 4C), and 98
(Fig. 4D) proteins dysregulated in *Ddx3x*^+/+^, *Ddx3x*^+/-^, *Ddx3x*^-/y^ neurons,
respectively. Using Fisher's exact test with Bonferroni correction, we
found that of the 193 proteins with a sex bias in expression, the 114
upregulated in female neurons converged on GO terms related to RNA
processing and mRNA translation terms (Fig. 4E). Intriguingly, the GO
results of the proteins dysregulated in *Ddx3x*^+/-^ when compared with
Ddx3x^+/+^ neurons offered a specular scenario, with an enrichment of
mRNA translation terms for downregulated proteins in *Ddx3x*^+/-^ neu-
rons (Fig. 4F). For example, proteins in the top enriched term "cyto-
plasmic translation" had higher expression in female neurons than
male neurons, but reduced expression in female neurons with *Ddx3x*
haploinsufficiency compared to control female neurons (Fig. 4E, F).
Among the proteins with reduced expression in *Ddx3x*^+/-^ compared to
Ddx3x^+/+^ neurons, were 5 tRNA synthetases, 5 ribosomal proteins of the
small 40S subunit, 3 initiation factors, 8 ribosomal proteins of the large
60S subunit (Fig. 4G), and 5 proteins involved in mitochondrial
translation (*Mrps18b, Mrpl24, Tufm, Mrps26, Mrps30*). The reduced

expression of two ribosomal proteins of the large subunit (*Rpl36a*;
Rpl11), one protein of the small subunit (*Rps5*) and a translation
initiation factor (*Eif3k*) in *Ddx3x*^+/-^ neurons was also validated by Wes-
tern blot (Fig. S4B, C). The brain-specific form of the translation ter-
mination factor eRF3[42], ERF3B (encoded by *Gspt2*), had enhanced
expression in *Ddx3x*^+/-^ neurons (Fig. 4G). The observed reduction in
ribosomal proteins aligns with findings in a *DDX3X* knockdown model
in lymphoma cell lines[43]. Strikingly, 7 of the 13 ribosomal proteins
reduced in *Ddx3x*^+/-^ neurons are encoded by mRNAs that were found
to interact with DDX3X based on iCLIP data in lymphoma cell lines [43]
(i.e., *Rps3, Rps5, Rps8, Rps19, Rpl11, Rpl13, Rpl30*), and 5 were found to
have reduced translational efficiency in the *DDX3X*
knockdown lymphoma model[43] (i.e., *Rps3, Rps5, Rps19, Rpl11, Rpl13*).
These data suggest that in cortical neurons *Ddx3x* regulates the
expression of core components of the protein synthesis machinery.

By contrast, we found no significant enrichment for the 98 pro-
teins dysregulated in *Ddx3x*^-/y^ compared with *Ddx3x*^+/y^ neurons. Several
of the proteins found dysregulated are indispensable for proper den-
dritic development, e.g. *Dcx*[44] and *Plxnd1*[45], or for neuronal migration,
e.g., *Rab23*[46] and *Fbxo45*[47]. This suggests that the overlapping mor-
phogenesis defects observed in *Ddx3x*^+/-^ and *Ddx3x*^-/y^ neurons (Fig. 1)
result from distinct molecular mechanisms. Further, the differentially
expressed proteins in *Ddx3x*^-/y^ neurons (but not those dysregulated in
Ddx3x^+/-^ neurons) were enriched for proteins encoded by targets of
two RNA-binding proteins associated with ID/ASD, FMRP and RBFOX
(Fig. S3D).

To gain insights on the disease relevance of our datasets
(Fig. 4B–D), we examined the intolerance to loss-of-function genetic
variation in their human orthologues using the well-established
metrics of loss-of-function observed/expected upper bound fraction
(LOEUF)[48] (Supplemental Note). Human orthologues of sex-biased
proteins and proteins dysregulated in *Ddx3x* mutant neurons, either
female or male, all displayed skewed distribution toward lower LOEUF
deciles (Fig. S3C), in keeping with the high genomic constraints for
genes expressed in brain. Also, human orthologues of the sex-biased
proteins included genes associated with severe neurodevelopmental
disorders (DDG2P[49] genes), ASD risk genes (ASC[50] genes), and/or epi-
lepsy (EPI[51–53] genes), albeit with no statistically significant enrichment.
For example, 18 proteins encoded by DDG2P genes had higher
expression in female neurons (e.g., *Ddx3x, Auh, Tufm*) and another 8
had higher expression in male neurons (e.g., *Napb, Shank2, Ank2*)
(Supplementary Data 1). 5 proteins encoded by ASC gene orthologues
had a sex bias in expression, and they all had higher expression in male
neurons (*Adcy5, Coro1a, Ank2, Shank2, Cul3*) (Supplementary Data 1).
30 proteins encoded by DDG2P gene orthologues had altered
expression in *Ddx3x*^+/-^ neurons, specifically 10 up-regulated proteins
(e.g., *Shank2, Nrxn3*) and 20 down-regulated proteins (e.g., *Auh,
Ccdc88a, Tufm*). 13 proteins encoded by DDG2P gene orthologues had
altered expression in *Ddx3x*^-/y^ neurons, specifically 7 up-regulated

A AAV8-EF1a-mCherry-IRES-Cre

E15 · DIV0 · DIV9

Genotype of all plated neurons: $Ddx3x^{+/+}$, $Ddx3x^{+/flox}$, $Ddx3x^{+/y}$, $Ddx3x^{flox/y}$

Genotype of homogenously infected neurons: $Ddx3x^{+/+}$, $Ddx3x^{+/-}$, $Ddx3x^{+/y}$, $Ddx3x^{-/y}$

B $Ddx3x^{+/+}$ (n=5) vs $Ddx3x^{+/y}$ (n=5)

C $Ddx3x^{+/-}$ (n=5) vs $Ddx3x^{+/+}$ (n=5)

D $Ddx3x^{-/y}$ (n=5) vs $Ddx3x^{+/y}$ (n=5)

E $Ddx3x^{+/+}$ vs $Ddx3x^{+/y}$

F $Ddx3x^{+/-}$ vs $Ddx3x^{+/+}$

G Translating polysomes

H $Sox2\text{-}Ddx3x^{+/-}$ (n=4) vs $Sox2\text{-}Ddx3x^{+/+}$ (n=4) — Synaptosomes

I -log10 Q-value

J $Ddx3x^{+/+}/Ddx3x^{+/y}$, $Ddx3x^{+/-}/Ddx3x^{+/y}$

proteins (e.g., *Dcx, Adsl, Shank1*) and 6 down-regulated proteins (e.g., *Rab23, Napb*).

To explore the molecular correlates of the altered dendritic spines in *Ddx3x^{+/-}* neurons, we delineated the proteomic profile of cortical synaptosomes purified from *Sox2-Ddx3x^{+/-}* and *Sox2-Ddx3x^{+/+}* female mice at postnatal day 21, a peak for synaptogenesis. As for prior

experiments, we restricted analyses to proteins identified with at least two unique peptides (see Methods) and proceeded to identify up- and down-regulated proteins (indicated in the figure and below with the gene names, Fig. 4H). When comparing *Ddx3x^{+/+}* and *Ddx3x^{+/-}* synaptosomes, we found 498 dysregulated proteins (Supplementary Data 2), specifically 147 proteins up-regulated and 351 down-regulated in

Fig. 4 | *Ddx3x* regulates the neuronal and synaptic proteome. A Experimental design. Cortical neurons are isolated from E15 embryos and transduced at DIV0 with AAV expressing mCherry and CRE, resulting in *Ddx3x*$^{+/+}$ (black), *Ddx3x*$^{+/-}$ (purple), *Ddx3x*$^{+/y}$ (gray), or *Ddx3x*$^{/y}$ (yellow) neurons. Analyses are performed at DIV14. Created in BioRender[103]. **B** Sex influences the neuronal proteome. Volcano plots of the proteomic data contrasting *Ddx3x*$^{+/+}$ and *Ddx3x*$^{+/y}$ neurons. FC, fold change; gray dotted line, *P*-value = 0.05. See Supplementary Data 1. **C** *Ddx3x* haploinsufficiency influences the neuronal proteome. As in **B**, contrasting *Ddx3x*$^{+/-}$ and *Ddx3x*$^{+/+}$ neurons. See Supplementary Data 1. **D** *Ddx3x* ablation in male neurons influences the neuronal proteome. As in B, contrasting *Ddx3x*$^{/y}$ and *Ddx3x*$^{+/y}$ neurons. See Supplementary Data 1. **E** Proteins with increased expression in female neurons converge on RNA processing and mRNA translation. Enriched GO terms for proteins upregulated (red) or downregulated (blue) in *Ddx3x*$^{+/+}$ neurons compared to *Ddx3x*$^{+/y}$ neurons (number of genes in each term on the Y axis; white dotted line, *P*-value = 0.05). **F** Proteins with reduced expression in *Ddx3x* haploinsufficient neurons converge on RNA processing and mRNA translation. As in

E, for proteins upregulated (red) or downregulated (blue) in *Ddx3x*$^{+/-}$ neurons compared to *Ddx3x*$^{+/+}$ neurons. **G** Proteins dysregulated in *Ddx3x* haploinsufficient neurons are involved in mRNA translation. Proteins (indicated by gene names) downregulated (blue) or upregulated (red) in *Ddx3x*$^{+/-}$ neurons compared to *Ddx3x*$^{+/+}$ neurons. Created in BioRender[104]. **H–I** *Ddx3x* haploinsufficiency changes the synaptic proteome. Volcano plot (**H**) and SynGO[55] enrichment plot (**I**) of the proteomic data on synaptosomes from P21 *Sox2-Ddx3x*$^{+/+}$ or *Sox2-Ddx3x*$^{+/-}$ mice. FC, fold change; gray dotted line, *P*-value = 0.05. In all panels, data were collected blind to genotype and sex; *n* is shown in legend as number of embryos (B-D) or P21 mice (H). See Supplementary Data 2. **J** *Ddx3x* haploinsufficiency obliterates the female bias in expression for 17 proteins. The plot shows the fold change for proteins listed on the Y axis by comparing *Ddx3x*$^{+/+}$ to *Ddx3x*$^{+/y}$ neurons or *Ddx3x*$^{+/-}$ to *Ddx3x*$^{+/y}$ neurons, based on the data in **B–D**. Proteins indicated by gene names; gray dotted line, reference expression in *Ddx3x*$^{+/y}$ neurons. See Supplementary Data 3. Source data are provided as a Source Data file.

Ddx3x$^{+/-}$ synaptosomes (Fig. 4H). *Ddx3x* was found to be expressed at synapses in line with a prior synaptic proteomic dataset[54] and, as expected, reduced in expression in *Ddx3x*$^{+/-}$ synaptosomes (Fig. 4H, Supplementary Data 2). As expected, the differentially expressed proteins were enriched in synaptic terms (Fig. 4I), as 114 of the 346 proteins dysregulated in *Ddx3x*$^{+/-}$ synaptosomes were bona fide synaptic proteins as defined by the SynGO consortium[55]. We then crossed the list of genes encoding the 498 differentially expressed proteins with the DDG2P genes[49], ASC genes[50], and EPI genes[51–53], and found a statistically significant enrichment for DDG2P genes (Fig. S3D). 84 were encoded by DDG2P genes, 9 by ASC genes (4 of which also captured by DDG2P; *Psmd12*, *Nrxn1*, *Scn2a*, and *Plxna1*), and 3 by EPI genes (all 3 captured by DDG2P genes, *Ube3a*, *Eef1a2*, and *Scn2a*). At the intersection of the differential expressed proteins, established SynGO genes, and disease risk genes are critical regulators of synaptic function, including *Dlg3*, *Nrxn1*, *Nrxn2*, *Scn2a*, *Cntnap2* and *Rac1*. When crossing the list of dysregulated proteins in *Ddx3x*$^{+/-}$ synaptosomes (Fig. 4H) and neurons (Fig. 4C), we found 19 shared proteins in addition to *Ddx3x*, including *Rpl22a* and *Ccdc88a* (also known as Girdin) (Fig. S3E).

These data map the molecular correlates of the deficits in neuronal morphogenesis (Figs. 1, 2) and dendritic spines (Fig. 3) caused by perturbations in *Ddx3x*, and show that there are sex-specific *Ddx3x* signatures, including alterations of ribosomal proteins and translational regulators exclusively in female neurons.

Ddx3x mediates sex dimorphisms in neuronal ribosome biogenesis

Compared to male neurons, female neurons have higher dosage requirements for *Ddx3x*, as it has evolved as an X chromosome escape gene[24,29,31]. Female neurons also display enhanced expression of components of the protein synthesis machinery (Fig. 4B–E). *Ddx3x*$^{+/-}$ neurons have dampened expression of ribosomal proteins compared to female control neurons (Fig. 4C–F). Therefore, we conjectured that *Ddx3x* might mediate the female-biased surplus of protein synthesis components.

To test this hypothesis, we verified if the higher expression of proteins in female neurons requires *Ddx3x*. We started by intersecting proteins with altered levels in *Ddx3x*$^{+/-}$ neurons (Fig. 4C) with those showing differential expression based on sex (Fig. 4B) and identified 37 proteins (Supplementary Data 3). We then filtered for proteins that have at least 30% higher expression in female neurons compared to male neurons (Expression$_{Ddx3x+/+}$/Expression$_{Ddx3x+/y}$ > 1.3) and identified 20 proteins. Of these 20, 17 have similar levels of expression when comparing female haploinsufficient neurons and male control neurons (Expression$_{Ddx3x+/-}$/Expression$_{Ddx3x+/y}$ = 1 ± 0.15), indicating that *Ddx3x* deficiency obliterates their female bias in expression (Fig. 4J, Supplementary Data 3). Six of these proteins are

downregulated in *Sox2-Ddx3x*$^{+/-}$ synaptosomes (*Auh*, *Tufm*, *Naxd*, *Acad8*, *Farsb*, and *Tfam*). Six proteins are also encoded by genes whose human orthologues are DDG2P genes (*TUFM*, *TFAM*, *NUP133*, *NAXD*, *FARSB*, and *AUH*) and one (*TUFM*) shows higher expression in human cortices from female donors than tissues from male donors (Fig. S3B). The remaining three proteins (*Rbm4b*, *Pds5b*, *Ssbp1*) do not meet these stringent criteria but show an attenuation of their sex bias (Supplementary Data 3). Of the 17 proteins with female-biased expression, five are implicated in mRNA translation (*Tufm*, *Rps3*, *Rpl11*, *Mrpl24*, *Farsb*) and another four are RNA-binding proteins (*Igf2bp1*, *Hnrnpf*, *Celf3*, *Auh*). *Rps3* and *Rpl11* were also detected in a DDX3X iCLIP dataset[43]. These data suggest that female neurons have higher expression of a set of ribosomal and translational regulators and that this female bias depends on the biallelic expression of *Ddx3x*.

We next sought to verify whether this signature resulted into changes in global protein synthesis rates. To this end, we performed a puromycin-based assay adapted from the SUnSET technique[56,57]. We trasduced DIV0 cortical neurons from *Ddx3x*$^{+/+}$, *Ddx3x*$^{+/flox}$, or *Ddx3x*$^{+/y}$ E15 embryos with AAV8-Ef1a-mCherry-IRES-Cre viral particles. At DIV9, we performed a 10-min puromycin pulse followed by a 30 min chase (Fig. S5A). This approach was effective in detecting newly synthesized proteins, as shown by abrogated puromycin incorporation in neurons treated with the protein synthesis inhibitor cycloheximide prior to the pulse (Fig. S5A, B). When comparing the three genotypes, we did not detect significant differences in the puromycin labeling (Fig. S5B, C), suggesting that there are no overt changes in global protein synthesis detectable with this approach.

We reasoned that the *Ddx3x*-dependent female bias might reflect more complex aspects of ribosome formation, which undergoes sophisticated forms of regulation in neural cells[21,58]. Therefore, we measured the abundance and subcellular distribution of ribosomal RNA (rRNA). Using a monoclonal antibody raised against the 5.8S rRNA (clone Y10b[58–65]), we quantified rRNA in the developing motor cortex of *Sox2-Ddx3x*$^{+/+}$, *Sox2-Ddx3x*$^{+/-}$, or *Sox2-Ddx3x*$^{+/y}$ neonates (Fig. 5A). Based on previous observations of altered layer V cortical neurons expressing the transcription factor CTIP2 in *Sox2-Ddx3x*$^{+/-}$ females[24], we conducted analyses in both CTIP2^{+} neurons and neighboring CTIP2^{-} cells (Fig. 5A–C). Irrespective of genotype, most rRNA was detected in the cytoplasm (Fig. 5B, C), as in previous reports[58–61]. In CTIP2^{+} neurons, the cytoplasm-to-nucleus ratio of the rRNA was ~87:13 % in *Sox2-Ddx3x*$^{+/+}$ females, but dropped to ~75:25 % in both *Sox2-Ddx3x*$^{+/-}$ and *Sox2-Ddx3x*$^{+/y}$ mice (Fig. 5B). The ratio was detected at ~75:25 % in CTIP2^{-} cells, irrespective of genotype (Fig. 5C). These observations suggest that female neurons might have a different rate of ribosomal maturation specifically in CTIP2^{+} neurons, and that this sex bias depends upon *Ddx3x*. We note that *Rpl11* is among the ribosomal proteins with higher expression in female neurons but reduced levels in *Ddx3x* haploinsufficient neurons (Fig. 4J,
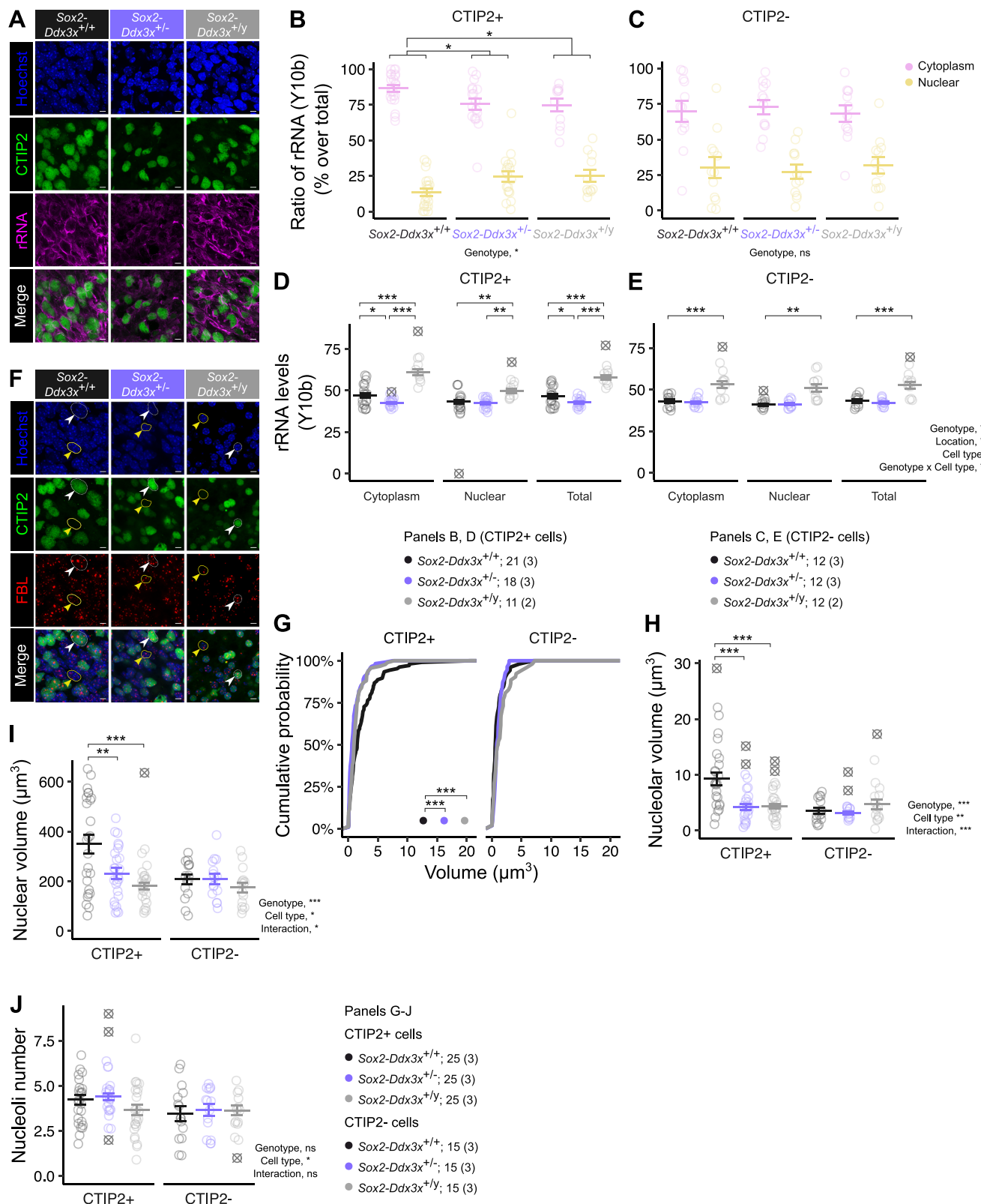
Panels B, D (CTIP2+ cells)
- *Sox2-Ddx3x*$^{+/+}$; 21 (3)
- *Sox2-Ddx3x*$^{+/-}$; 18 (3)
- *Sox2-Ddx3x*$^{+/y}$; 11 (2)

Panels C, E (CTIP2- cells)
- *Sox2-Ddx3x*$^{+/+}$; 12 (3)
- *Sox2-Ddx3x*$^{+/-}$; 12 (3)
- *Sox2-Ddx3x*$^{+/y}$; 12 (2)

Panels G-J

CTIP2+ cells
- *Sox2-Ddx3x*$^{+/+}$; 25 (3)
- *Sox2-Ddx3x*$^{+/-}$; 25 (3)
- *Sox2-Ddx3x*$^{+/y}$; 25 (3)

CTIP2- cells
- *Sox2-Ddx3x*$^{+/+}$; 15 (3)
- *Sox2-Ddx3x*$^{+/-}$; 15 (3)
- *Sox2-Ddx3x*$^{+/y}$; 15 (3)

Fig. S4B, C) and that this protein has a critical role in pre-ribosome assembly[66,67].

When quantifying the mean rRNA expression, male neurons had overall higher rRNA levels than female neurons, for both CTIP2$^+$ and CTIP2$^-$ cells (Fig. 5D, E). Put together with the cytoplasm-to-nucleus ratio, these results suggest sex differences in ribosome biogenesis, where higher rates of ribosome export/maturation are preferred in

CTIP2$^+$ neurons in females and an overall higher production of ribosomes is more favorable in males. Further, the CTIP2$^+$ neurons from *Sox2-Ddx3x*$^{+/-}$ neonates have a ~15% net reduction in rRNA (Fig. 5D). These observations suggest that *Ddx3x* mutations in neurons are associated with altered rRNA expression and ribosomal deficits.

As canonical ribosome biogenesis takes place in the nucleolus, we conjectured that sex and *Ddx3x* dosage might alter the nucleoli. To test

Fig. 5 | _Ddx3x_ mediates a female bias in ribosome biogenesis. A–E _Ddx3x_ regulates ribosome dynamics in CTIP2-expressing cortical neurons. A Confocal images of layer V from the developing primary motor cortex of _Sox2-Ddx3x_$^{+/+}$ (black), _Sox2-Ddx3x_$^{+/-}$ (purple), and _Sox2-Ddx3x_$^{+/y}$ (gray) neonate immunostained for CTIP2 (green), rRNA (magenta, Y10b antibody[58–65]), and Hoechst (blue). Scale bar, 5 µm. **B, C** The plots show the percentage of rRNA in cytoplasm (pink) or nucleus (yellow) over the total rRNA in CTIP2$^+$ (**B**) or CTIP2$^-$ (**C**) cells. **D–E** The plots show the cytoplasmic, nuclear, and total levels of rRNA (as mean Y10b immunofluorescence) in CTIP2$^+$ (**D**) or CTIP2$^-$ (**E**) cells. **F–H** _Ddx3x_ regulates nucleolar properties in CTIP2-expressing cortical neurons. Representative image of layer V in the developing primary motor cortex from _Sox2-Ddx3x_$^{+/+}$, _Sox2-Ddx3x_$^{+/-}$, and _Sox2-Ddx3x_$^{+/y}$ neonates stained for Hoechst (blue), CTIP2 (green), fibrillarin (FBL, red). White arrowheads, example of CTIP2$^+$ neurons; yellow arrowheads, example of CTIP2$^-$ cells. Scale bar, 5 µm. **G–H** Empirical cumulative distribution function of the nucleoli volume (**G**) and sum volume of all the nucleoli per cell (**H**). **I** The nuclei of CTIP2$^+$ neurons are larger in female neurons, but not if they have _Ddx3x_ monoallelic expression. The plot shows the total nuclear volume per cell. **J** The number of nucleoli does not differ by genotype. The plot shows the average number of nucleoli per cell. Statistics: Panels **B**, **C**, one-way ANOVA, followed by Student's t test with Benjamini-Hochberg correction; Panel **D**, **E**, three-way ANOVA, followed by Student's t test with Benjamini-Hochberg correction; Panel **G**, Kolmogorov–Smirnov test; Panels **H**, **I**, two-way ANOVA, followed by Student's t test with Benjamini-Hochberg correction; Panel **J**, Kruskal-Wallis test, followed by Wilcoxon test with Benjamini-Hochberg correction. In all panels, data were collected blind to genotype and sex; mean ± SEM; outliers shown as ⊗; *P-value < 0.05, **P-value < 0.01, ***P-value < 0.001. Source data are provided as a Source Data file.

this hypothesis, we examined the number and volume of nucleoli in cortical neurons from the developing motor cortex of _Sox2-Ddx3x_$^{+/+}$, _Sox2-Ddx3x_$^{+/-}$, and _Sox2-Ddx3x_$^{+/y}$ neonates using the nucleolar marker fibrillarin[59,62,68] (Fig. 5F). When compared to their male counterparts, CTIP2$^+$ female neurons had on average larger nucleoli (Fig. 5G) and higher total nucleolar volume (Fig. 5H), without changes in the number of nucleoli (Fig. 5J). CTIP2$^+$ female neurons also had larger nuclei than male neurons and female haploinsufficient neurons (Fig. 5I). The specificity of these differences for CTIP2$^+$ neurons goes hand in hand with the _Ddx3x_-dependent female bias toward higher repartitioning of cytoplasmic ribosomes (Fig. 5B, C), corroborating that ribosome biogenesis differ in female and male neurons via pathways that depend on _Ddx3x_ biallelic expression.

We examined nucleolar measures also in cultured cortical neurons, which are mostly expressing CTIP2 (Fig. S6A). We found that the _Ddx3x_-dependent female bias manifested in the number of nucleoli, and that _Ddx3x_$^{/y}$ neurons did not show changes in nucleoli compared with male controls (Fig. S6B–F). We note that although there is convergence in a _Ddx3x_-dependent female-biased nucleolar signature ex vivo (Fig. 5) and in vitro (Fig. S6B–F), the nature of this signature differs. These differences might result from the fact that the _Ddx3x_ deletion in the cultured system ensues at E15, plausibly post-mitotically, while it starts at gastrulation (thus also in the neural progenitors) in _Sox2-Ddx3x_$^{+/-}$ mice.

Altogether, these data show that biallelic expression of _Ddx3x_ in female neurons is required to impart sexually dimorphic characteristics and that _Ddx3x_ haploinsufficiency results in deficits in nucleolar properties and ribosome biogenesis.

DDX3X and its paralog DDX3Y have only partially redundant functions in neuronal development

The data so far show that _Ddx3x_ shapes sexual differentiation during neuronal development. This might result from unbalanced expression with _Ddx3y_ and/or divergent molecular properties. To eliminate dosage as a variable and formally assessed functional redundancy, we exogenously expressed human DDX3X (hDDX3X) or DDX3Y (hDDX3Y) in _Ddx3x_$^{+/-}$ neurons (Fig. 6A). Further, to verify that potential hDDX3X-induced phenotypes could be circumscribed to its catalytic functions, we used an ATPase-deficient mutant (E348Q)[69–71] (Fig. 6A).

Cortical neurons were isolated from E15 _Ddx3x_$^{+/flox}$ embryos and transfected with the pAAV-Ef1a-mCherry-IRES-Cre with or without expression vectors carrying tagged hDDX3X, hDDX3Y, or hDDX3X-E348Q (Fig. 6A). This genetic manipulation resulted in sparse mCherry$^+$ haploinsufficient neurons (_Ddx3x_$^{+/-}$), mCherry$^+$HA$^+$ haploinsufficient neurons co-expressing hDDX3X (_Ddx3x_$^{+/hDDX3X}$), mCherry$^+$HA$^+$ haploinsufficient neurons co-expressing the ATPase-deficient hDDX3X (_Ddx3x_$^{+/E348Q}$), or mCherry$^+$FLAG$^+$ haploinsufficient neurons co-expressing hDDX3Y (_Ddx3x_$^{+/hDDX3Y}$) (Fig. 6A, B). We then examined dendritic development and nucleolar properties, in keeping with the design of our previous analyses (Figs. 1, 2, 5, Fig. S6B–F).

We found that hDDX3X or hDDX3Y alleviated the dendritic deficits observed in _Ddx3x_$^{+/-}$ neurons (Fig. 6B, C). Co-expression of hDDX3X or hDDX3Y significantly increased nucleolar volume (Fig. 6D–F) but had divergent effects on the number of nucleoli (Fig. 6G). In fact, _Ddx3x_$^{+/hDDX3Y}$ showed a number of nucleoli comparable to _Ddx3x_$^{+/-}$ neurons, but _Ddx3x_$^{+/hDDX3X}$ had a significant reduction compared to all other genotypes (Fig. 6G). The lack of effect of hDDX3Y on the number of nucleoli is compatible with the lack of a nucleolar phenotype in _Ddx3x_$^{/y}$ neurons (Fig. S6). Nuclear features remained unaltered across all genotypes (Fig. 6H). Co-expressing hDDX3X-E348Q had no effect on any of the measures (Fig. 6B, C). Considering that the nucleolus is a phase-separated organelle, our data align with prior evidence showing that human DDX3X and DDX3Y have distinct propensities to LLPS[15,18,19].

This body of findings demonstrates that intact catalytic activity is required for DDX3X to regulate neuronal morphogenesis and nucleolar dynamics, and that the balance between DDX3X and DDX3Y resides in both their expression and function.

Loss of Ddx3x in the forebrain leads to developmental delays and adult motor deficits

We then next sought to assess whether the interaction between _Ddx3x_ dosage and sex observed at the molecular and cellular level translates into behavioral outcomes.

Complete knockout of _Ddx3x_ is incompatible with life in male mice[24,26], while _Sox2-Ddx3x_$^{+/-}$ females have postnatal motor delays, adult motor deficits, hyperactivity, anxiety-related behaviors, and cognitive impairments[24]. To be able to compare female and male mutant mice, we selected a forebrain-conditional _Ddx3x_ knock-out model, based on clinical observations[2,3,5] and evidence in mouse models[3,12,24] (including those presented here) showing that forebrain neurons are particularly vulnerable to _DDX3X_ mutations. We crossed the _Ddx3x_^{flox} line with an _Emx1_$^{IRES-Cre}$ driver line that expresses the CRE recombinase under the endogenous _Emx1_ promoter in the telencephalon as early as E10.5[72,73]. We obtained four genotypes: _Emx1-Ddx3x_$^{+/+}$ control females, _Emx1-Ddx3x_$^{+/-}$ haploinsufficient females, _Emx1-Ddx3x_$^{+/y}$ control males, and _Emx1-Ddx3x_$^{/y}$ null males. As intended, _Emx1-Ddx3x_$^{/y}$ null males show loss of DDX3X in the forebrain, but not in the midbrain or hindbrain (Fig. 7A). _Emx1-Ddx3x_ mutants were born at the expected mendelian ratio, did not show reduced viability from birth to the postnatal day 21, and survived to adulthood.

Emx1-Ddx3x$^{/y}$ null males showed delayed growth over the first four weeks of life (Fig. 7B) which then normalized in adulthood (Fig. 7C). _Emx1-Ddx3x_$^{/y}$ null males showed no major physical (Fig. S7), sensory (Fig. S8), or motor (Fig. S9) developmental delays, but had a statistically significant delay in the eruption of the top tooth (Fig. S7D), and the acquisition of motor abilities such as grip strength (Fig. S9E) and air righting (Fig. S9F) showed a distinct trajectory over time. The developmental trajectory of the _Emx1-Ddx3x_$^{+/-}$ heterozygous females was mostly indistinguishable from that of their control littermates (Fig. 7B, Fig. S7–9), except for precocious development of the forelimb
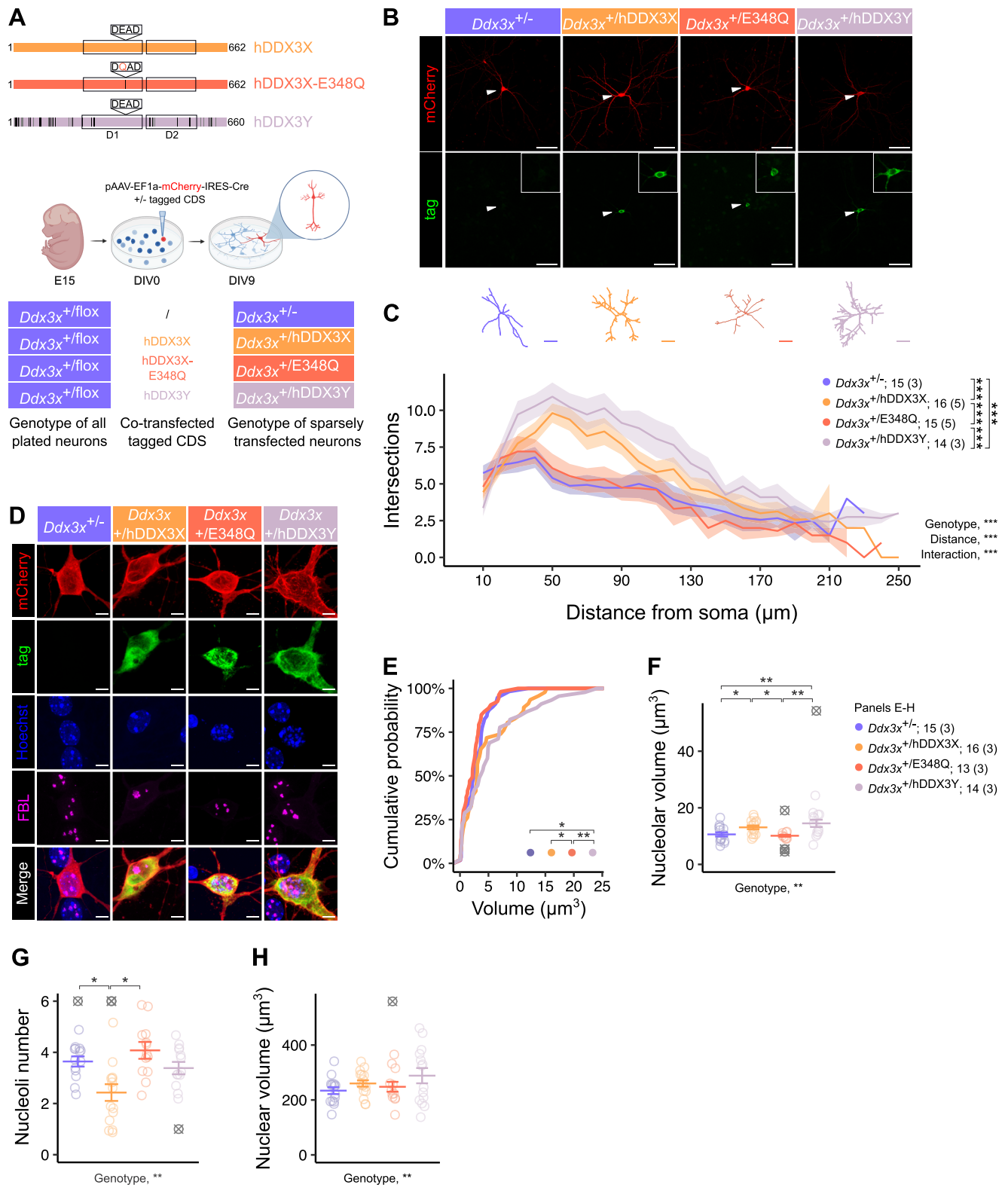
grasp reflex which then reached a plateau (Fig. S8B). Further, both *Emx1-Ddx3x*[-/y] and *Emx1-Ddx3x*^{+/-} juvenile mice displayed subtle changes suggestive of a wider gait, appearing at P22 in *Emx1-Ddx3x*^{+/-} and only at P30 in *Emx1-Ddx3x*[-/y] males (Fig. S10). This is in contrast with what we previously observed in *Sox2-Ddx3x*^{+/-} mice, which showed a reduction in horizontal and diagonal parameters at P22, resolved by P30[24]. Collectively, these data indicate that the previously reported developmental delays observed in the global *Sox2-Ddx3x* model are

not exclusively dependent on the forebrain, and that nevertheless there is an interaction between sex and genotype and/or a complex dosage effect, as some phenotypes are detected in haploinsufficient females but not in null males (Figs. S8B, S10).

Among the most clinically salient phenotypes observed in the *Sox2-Ddx3x* mouse model are motor delays and poor motor coordination and balance[24], reminiscent of the pervasive motor manifestations in individuals with DDX3X syndrome[2,3,5]. Further, corticopontine

Fig. 6 | The functions of DDX3X in dendritogenesis and ribosome biogenesis depend on its catalytic activity and are partially redundant with DDX3Y.
A Experimental design. Cortical neurons are isolated from *Ddx3x*[+/flox] E15 embryos and transfected at DIV0 with the construct carrying mCherry and CRE, with or without the expression vector harboring with the coding sequence (CDS) of human wild-type DDX3X (hDDX3X; HA-tagged; orange), ATPase-deficient E348Q mutant (hDDX3X-E348Q; HA-tagged; coral), or DDX3Y (hDDX3Y; FLAG-tagged; light purple; non-identical residues to hDDX3X shown in gray). Analyses are performed at DIV9. Created in BioRender[103]. **B** Validation of the *Ddx3x* manipulations. Confocal images of DIV9 neurons immunostained for mCherry (red) and HA/FLAG tag (green). Scale bar, 50 μm. **C** Deficits of dendritic arborization caused by *Ddx3x* haploinsufficiency are alleviated by DDX3X or DDX3Y but not by an ATPase-deficient DDX3X. The plot shows the number of branching points as a function of the distance from the soma in DIV9 neurons. Representative traces shown on top. Scale bar, 5 μm. **D** DDX3X or DDX3Y differ in their impact on nucleolar properties,

while ATPase-deficient DDX3X has no effect. Confocal images of DIV9 neurons immunostained for mCherry (red), CTIP2 (green), HA/FLAG tag (green), and Hoechst (blue). Scale bar, 5 μm. **E, F** Expression of DDX3X or DDX3Y induces larger nucleoli, while ATPase-deficient DDX3X has no impact. The plot shows the empirical cumulative distribution function of the nucleoli volume (**E**) or the sum volume of all the nucleoli (**F**). **G** DDX3X, but not DDX3Y, affects the number of nucleoli. The plot shows the total number of nucleoli per cell. **H** DDX3X or DDX3Y expression does not alter nuclear volume. The plot shows the total nuclear volume per cell. Statistics: Panel **C**, repeated measure ANOVA, followed by Tukey test with Benjamini-Hochberg correction; Panel **F** and **H**, One-way ANOVA, followed by Student's t test with Benjamini-Hochberg correction; Panel **E**, Kolmogorov–Smirnov test; Panel **G**, Kruskal-Wallis test, followed by Wilcoxon test with Benjamini-Hochberg correction. In all panels, data were collected blind to genotype and sex; mean ± SEM; outliers shown as ⊗; *P-value < 0.05, **P-value < 0.01, ***P-value < 0.001. Source data are provided as a Source Data file.

---

neurons, which are engaged in critical motor circuits, have dendritic alterations when *Ddx3x* is mutated (Fig. 2). Therefore, we assessed motor function in the *Emx1-Ddx3x* mutant line. During handling one week prior to behavioral testing, we noted no differences in physical appearance or weight (Fig. 7C). In terms of baseline activity, we observed reduced inverted screen performance for both *Emx1-Ddx3x*^{+/-} and *Emx1-Ddx3x*[-/y] mutants compared to controls (Fig. 7D), and reduced number of jumps during spontaneous activity monitoring for *Emx1-Ddx3x*^{+/-} females (Fig. S11B), but no other changes (Fig. S11A, S11C–E).

To assess neuromuscular strength, we employed a wire hanging test (Fig. 7E, F). We detected a significant effect of genotype on performance, with *Emx1-Ddx3x*[-/y] null males showing reduced latency to fall from the wire when compared to male littermates (Fig. 7E), similar to the reduced endurance observed in *Sox2-Ddx3x*^{+/-} mice[24]. To assess motor coordination and balance, we used a balance beam test and a vertical pole test. When walking on the balance beam, control females covered a larger distance on the beam (Fig. 7G) than male littermates, plausibly because of their lower body weight (Fig. 7C). In line with observations in *Sox2-Ddx3x*^{+/-} mice[24], *Emx1-Ddx3x*^{+/-} covered a shorter distance on the beam than control female littermates (Fig. 7G). No differences in the number of slips or latency were noted (Fig. S12A, B). No sex or genotype differences were observed when mice were climbing down a vertical pole (Fig. S12C, D), in contrast to previous findings of impairments in this motor task in *Sox2-Ddx3x*^{+/-} mice[24]. To further test motor coordination and endurance and extend on motor learning, we used the accelerating rotarod test, with a design of four trials each day, over three days. In line with the outcomes of the balance beam test (Fig. 7G), control females outperformed male littermates (Fig. 7H). While *Emx1-Ddx3x*^{+/-} females were able to learn the task, they showed reduced performance compared to control females (Fig. 7H). *Emx1-Ddx3x*[-/y] males showed both impaired learning and coordination when compared to control males (Fig. 7H).

These observations are consistent with the defects in corticopontine neurons (Fig. 2), indicate that *Ddx3x* deficiency in the forebrain is sufficient to produce motor sequelae reminiscent of those found in the patient population[74], and reaffirm the complex sex-by-dosage interactions for the *Ddx3x* locus.

Discussion

By virtue of its nature as an X chromosome inactivation escapee[29], *DDX3X* is one of the top 15 female-biased genes in the human cortex[30] (Fig. S3), and one of the top 5 proteins with higher expression in female cortical murine neurons (Fig. 4B, Supplementary Data 1). Despite the dramatic Y chromosome decay during evolution, *DDX3X* and another 18 escapee genes have retained Y homologues[32], suggesting that the equilibrium between the X and Y partners (or the lack thereof) contributes to shape sex dimorphisms[33,35].

Our study provides evidence that *Ddx3x* acts as a mediator of sexual differentiation during brain development. First, we show that *Ddx3x* is necessary for the expression of a female-biased molecular and cellular signature associated with ribosome biogenesis (Figs. 4–6). Second, *Ddx3x* is indispensable for the formation and maturation of dendritic spines in female neurons only, as spines of male control or null neurons are indistinguishable (Fig. 3). Third, female mice outperform males in two motor tasks, but this sex advantage is lost in *Ddx3x* mutant females (Fig. 7). These data, combined with evidence in the literature, support a scenario whereby DDX3X and DDX3Y have evolved to have only partially redundant functions[15,18,19], in addition to a divergent expression pattern[37,39,41]. In fact, human DDX3X and DDX3Y differ in their catalytic properties and propensity to LLPS[15,18,19]. Coherently, they have distinct impact on nucleoli (Fig. 6). Further, unlike other X-Y pairs, DDX3X and DDX3Y can reciprocally regulate their dosage, likely as a result of inheriting high dosage sensitivity from their common autosomal ancestor[75]. In fact, in line with previous data in mouse models[12,25], we detect DDX3Y protein expression in male neurons when *Ddx3x* is silenced (Fig. S4A, Supplementary Data 1). Nevertheless, *DDX3Y* is unable to compensate for *DDX3X* during neurodevelopment, as evidenced by male cases with pathogenic *DDX3X* mutations[2,3,5,8] and the molecular (Fig. 4), cellular (Fig. 1), and behavioral (Fig. 7) sequalae of *Ddx3x* loss in males.

Our observations add a layer of complexity to the molecular alterations resulting from *DDX3X* haploinsufficiency in neurons. DDX3X has been postulated to act at the step of translational initiation and facilitate the translation of a subset of mRNAs with 5'UTRs bearing complex secondary structures through its helicase activity[10,11]. Our data in neurons show distinct molecular signatures based on sex. *Ddx3x* loss in male neurons results in a distinct and narrowed impact on proteins directly necessary for neurite outgrowth (Fig. 4), with no noticeable nucleolar alterations (Fig. S6B–F). *Ddx3x* haploinsufficiency in female neurons causes a downregulation of constitutive components of the protein synthesis machinery (Fig. 4, Fig. S4B, C), orthogonally corroborated by a reduction in rRNA and nucleoli volume (Fig. 5). Whether *Ddx3x* haploinsufficiency also impacts the processing and maturation of rRNAs remains to be examined. The ribosomal deficits might in turn alter the synthesis of specific proteins required to sustain dendritic growth, yielding the reduced dendritic branching resulting from *Ddx3x* perturbations (Figs. 1, 2).

The implications of our findings relating *Ddx3x* to ribosome biogenesis are twofold. First, ribosome biogenesis is dynamically regulated during cortical development[21,62,76] and protein synthesis rate is an inherent feature of cortical neuronal subtype[23]. The evidence of a *Ddx3x*-dependent female bias in ribosome biogenesis in CTIP2-expressing cortical neurons introduces a new player (*Ddx3x*) and a new variable (sex). More broadly, our study adds on an ever-evolving landscape of mechanisms of protein synthesis in
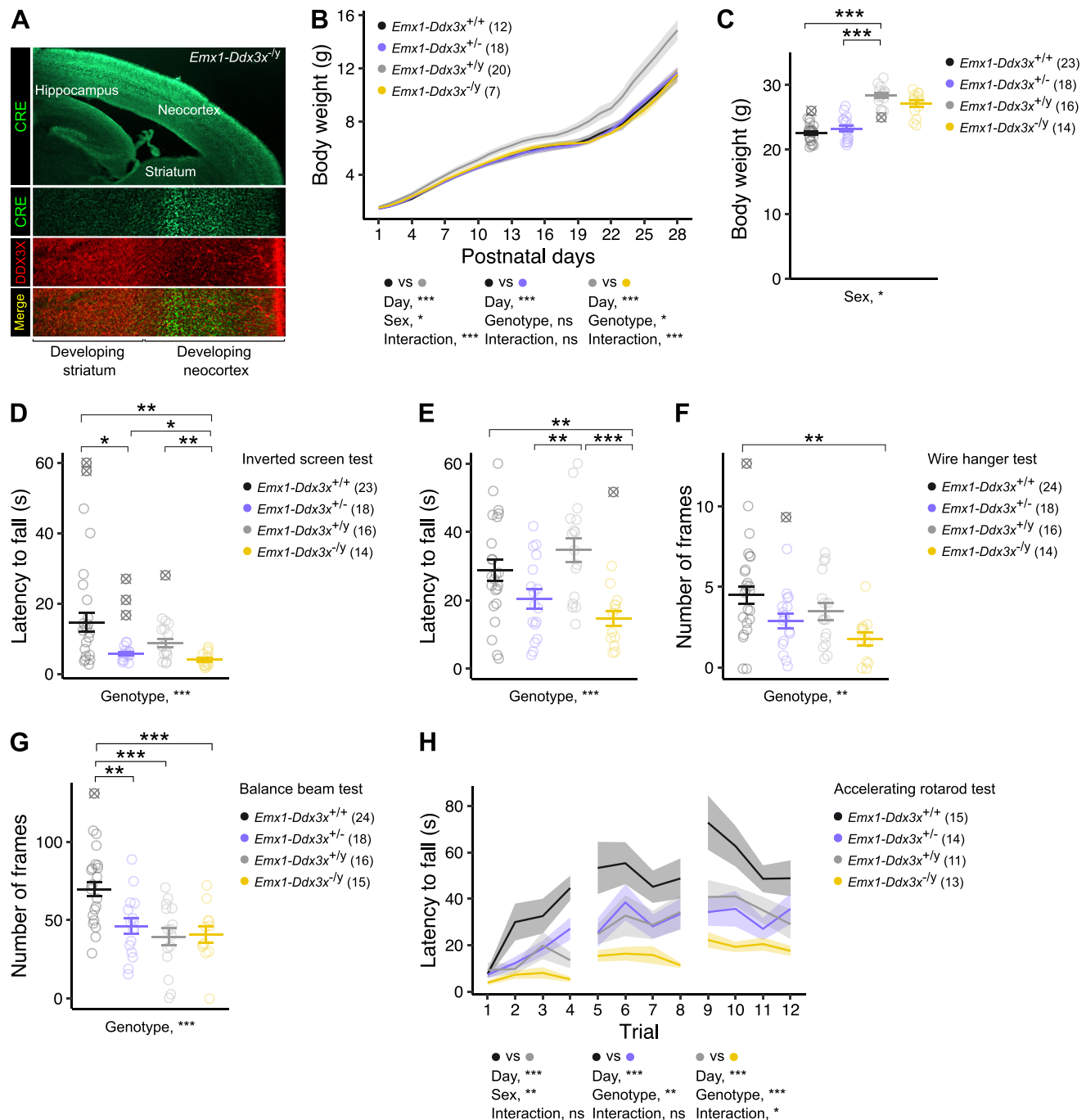
Fig. 7 | *Ddx3x* loss in the forebrain causes adult motor deficits. A Validation of the *Emx1-Ddx3x* knock-out mouse line. Confocal images of a E18.5 section from an *Emx1-Ddx3x*$^{-/y}$ null mouse, showing CRE (green) exclusively in the forebrain, with corresponding loss of DDX3X (red). **B** *Emx1-Ddx3x* null pups have delayed postnatal growth. Growth curves for *Emx1-Ddx3x*$^{+/+}$ control females (black), *Emx1-Ddx3x*$^{+/-}$ haploinsufficient females (purple), *Emx1-Ddx3x*$^{+/y}$ control males (gray), and *Emx1-Ddx3x*$^{-/y}$ null males (yellow). **C** *Emx1-Ddx3x* null males no longer display lower body weight as adults. The plot shows the body weight in adult mice across the four genotypes. **D** *Ddx3x* loss causes reduced grip in inverted screen test, when compared with *Emx1-Ddx3x*$^{+/+}$ female and *Emx1-Ddx3x*$^{+/y}$ male controls. **E, F** *Ddx3x* loss reduces endurance in wire hanger test, as measured by latency to fall (**E**) and

number of frames (**F**). **G** Sex and *Ddx3x* dosage in the forebrain affect performance on balance beam test, measured as number of frames walked. **H** Sex and *Ddx3x* dosage in the forebrain affect performance on an accelerating rotarod, measured as latency to fall. Statistics: Panels **B** and **H**, repeated measure ANOVA for the comparisons shown below the plot; Panels **C**, **D**, Kruskal–Wallis test, followed by Wilcoxon signed-rank test with Benjamini-Hochberg correction; Panels **E**–**G**, one-way ANOVA, followed by Student's t test with Benjamini-Hochberg correction. In all panels, data were collected blind to genotype and sex; *n* is shown in legend as number of mice; mean ± SEM; outliers shown as ⊗; *P-value < 0.05, **P-value < 0.01, ***P-value < 0.001. Source data are provided as a Source Data file.

neurons, where ribosomes have distinct conformations[77], specific co-regulators[78], and non-canonical mechanisms of biogenesis[58]. Second, a class of genetic conditions caused by mutations in proteins regulating LLPS and resulting in nucleolar alterations has

emerged[68]. Our findings suggest that DDX3X syndrome belongs to this group of disorders.

Our findings have direct relevance for our understanding of how neurodevelopment goes awry when *DDX3X* is mutated, by adding to

the clinical[2,3,5] and functional[3,12,24] data indicating that forebrain neurons, particularly in the cortex, are exquisitely vulnerable to perturbations in *DDX3X*. We show that *Ddx3x* expression in the forebrain is required for intact development and function of neurons engaged in motor circuits, as *Ddx3x*-deficient corticopontine neurons have altered dendritic arborization (Fig. 2) and forebrain-conditional *Ddx3x* mutant mice have motor deficits, although with significant sex differences (Fig. 7). We also show that *Ddx3x* is needed for the development of cortical neurons post-mitotically, in line with a previous report[27], thus expanding the window of risk for *DDX3X* mutations beyond prenatal development[3,12]. Synaptic function, in particular, has been pinpointed as a major nexus of risk for ASD[79], and genetically engineered mouse models for ASD have also shown deficits in synaptic development[80–83]. Importantly, dendritic growth, de novo synapse formation, and synapse maturation continue to be plastically reshaped during postnatal periods, including in response to experience[84–86], thus offering a more feasible window for therapeutic intervention. Our previous data[24] lend support for potential benefits of intervening postnatally on *Ddx3x* mutant mice. In fact, we found that one-year old *Sox2-Ddx3x*^{+/-} mice have more profound motor deficits than naïve 4-month-old *Sox2-Ddx3x*^{+/-} mice, but this decline is no longer seen in one-year old mice pre-exposed to behavioral training at 4 months of age. These data suggest that there might be mechanisms maintaining the pathological status (perhaps through the synaptic cellular and molecular alterations we found) that could be manipulated postnatally. This might add to the growing body of evidence showing that restoring expression/ function of some ASD risk genes in adult mice can alleviate their molecular and/or behavioral deficits[87–91]. Future studies will be critical to understand how the molecular and cellular alterations identified in this study can be targeted for the development of novel therapeutics for DDX3X syndrome.

Methods

Mouse lines
All animal procedures were approved by the Institutional Animal Care and Use Committee of the Icahn School of Medicine at Mount Sinai. To generate the neuronal cultures, we crossed *Ddx3x*[flox/+] females[24] with wild-type *Ddx3x*[+/y] males or *Ddx3x*[flox/y] males. To generate the *Sox2-Ddx3x* mice, *Ddx3x*[flox/flox] females were crossed with B6.Cg-Edil3[Tg(Sox2-Cre)1Amc]/J males (Sox2-Cre/+)[92] (The Jackson Laboratory, stock number #008454). To generate the *Emx1-Ddx3x* mice, *Ddx3x*[flox/flox] females were crossed with B6.129S2-*Emx1*[tm1(cre)Krj]/J (Emx1[IRES-Cre]/+) hemizygous males[72,73] (The Jackson Laboratory, stock number #005628). The colony was maintained in a room on a 12/12 h light/dark cycle, with lights on at 7 A.M. at a constant temperature of 21-22 °C and 55% humidity. Standard rodent chow and potable water were available *ad libitum*. Animals were socially housed, with 3-5 mice per cage. Mice were weaned at P21. The colony was maintained on a C57BL/6 J background. Genotyping is described in the Supplemental Note.

Primary cortical cultures
Cultures were prepared from E15 single embryos with a modified protocol[93]. Cortices were isolated in ice-cold Hank's balanced salt solution (HBSS) and then digested with pre-warmed papain containing DNase (Worthington, #LK003150) at 37 °C and 5% CO_2 for 30 minutes. Tissue chops were washed 3 times with Neuronal Plating Medium and then centrifuged for 3 minutes at 400 g. Mechanical dissociation was then performed in 1 ml of pre-warmed Neurobasal Medium (Thermo Fisher Scientific, #21103049). Cell density was determined with the Countess Automated Cell Counter (Thermo Fisher Scientific), with a yield on the order of 3-4 ×10^6 cells per embryo. Irrespective of timing of transfection/infection (see below), cells were maintained in Neuronal Plating Medium, and 90 minutes after plating the medium was replaced with pre-warmed Neurobasal Plus (Thermo Fisher Scientific, #A3582901) supplemented with B27 Plus (Thermo Fisher Scientific,

#A3582801). At DIV4, cells were treated with 1 μM cytosine arabinoside (1-b-D-arabinofuranosylcytosine (Sigma-Aldrich Inc, #C1768). Genotyping is described in the Supplemental Note.

DNA transfections
For dendritic arborization analyses in Fig. 1, 2 x 10^5 cells were incubated for 1 h in a 50 μl of Neurobasal containing 0.5 μl of Lipofectamine (Thermo Fisher Scientific, #11668019) and 500 ng of pAAV-Ef1a-mCherry-IRES-Cre (Addgene, #55632) in 1.5 ml conical tubes right before plating (DIV0) and then seeded onto poly-L-lysine-coated coverslips in 24-well plates containing Neuronal Plating Medium. Coverslips were fixed (see below) at DIV9. For dendritic spines analyses (Fig. 3), 1.5 ×10^5 neurons were plated at DIV0 onto poly-L-lysine-coated coverslips in 24-well plates containing Neuronal Plating Medium and then transfected at DIV9 by adding 100 μl of Neurobasal containing 0.75 μl of Lipofectamine and 500 ng of pAAV-Ef1a-mCherry-IRES-Cre directly onto each well. Coverslips were fixed (see below) at DIV14. For analyses in Fig. 6, DIV0 2 ×10^5 cells were incubated for 1 h in a 100 μl of Neurobasal containing 0.5 μl of Lipofectamine (Thermo Fisher Scientific, #11668019), and 500 ng of pAAV-Ef1a-mCherry-IRES-Cre (Addgene, #55632) with or without pCI-Neo-HA-DDX3X, pCI-Neo-HA-DDX3X-DQAD (E348Q), or pTWIST-CMV-FLAG-DDX3Y, in 1.5 ml conical tubes and then seeded onto poly-L-lysine-coated coverslips in 24-well plates containing Neuronal Plating Medium. Coverslips were fixed (see below) at DIV9. For nucleoli analyses in Fig. S6, DIV0 2 × 10^5 cells were incubated for 1 h in a 100 μl of Neurobasal containing 0.5 μl of Lipofectamine (Thermo Fisher Scientific, #11668019), and 500 ng of pAAV-Ef1a-mCherry-IRES-Cre or 500 ng of a control pAAV-Ef1a-mCherry (Addgene, #114470). Coverslips were fixed (see below) at DIV9.

Adeno-associated virus transductions
For analyses in Fig. 4, 10^6 cells were directly plated onto poly-L-lysine-coated 35 mm Petri dishes containing Neuronal Plating Medium, and cells were then transduced with 1 μl of AAV8-Ef1a-mCherry-IRES-Cre (Addgene, #55632-AAV8, 1 × 10^{13} vg/ml, multiplicity of infection (MOI) of 10,000). Cells were harvested at DIV9 (see below).

Immunostaining on cultured neurons
At DIV9 (Figs. 1, 6, Fig. S6A–F) or DIV14 (Fig. 3), coverslips were washed with pre-warmed 1X phosphate buffered saline (PBS) and fixed with a pre-warmed solution of 4% paraformaldehyde (PFA) /4% sucrose in 1X PBS at room temperature (RT) for 10 minutes. Coverslips were then washed once with 50 mM glycine in 1X PBS and twice with 1X PBS /0.1% Triton X-100 at RT for 5 minutes, and then treated with 1X PBS/0.3% Triton X-100 for 20 minutes to allow permeabilization. After blocking in 10% donkey serum/1X PBS /0.1% Triton X-100 for 1 h at RT, coverslips were incubated with goat anti-mCherry polyclonal antibody (SICgen antibodies, #AB0040, 1:200), a rabbit anti-DDX3X polyclonal antibody (Thermo Fisher Scientific, #A300-474A, 1:400), a rabbit anti-Fibrillarin polyclonal antibody (Abcam, #ab5821, 1:2,000), a mouse anti-HA-Tag (6E2) monoclonal antibody (Cell Signaling, #2367, 1:100), a mouse anti-FLAG M2 monoclonal antibody (Sigma-Aldrich, #F3165, 1:100), a rat anti-CTIP2/BCL11B monoclonal antibody (Millipore, #MABE1045, 1:300), and/or Hoechst dye (Thermo Fisher Scientific, #H3570, 1:1,000), diluted in blocking solution overnight at 4 °C. Coverslips were then washed 3 times with 1X PBS and incubated for 1 h at RT with a donkey anti-rabbit antibody conjugated with Alexa Fluor 647 (Thermo Fisher Scientific, #A-31573, 1:200), a donkey anti-goat antibody conjugated with Alexa Fluor 568 (Thermo Fisher Scientific, #A-11057, 1:200), a donkey anti-mouse antibody conjugated with Alexa Fluor 488 (Thermo Fisher Scientific, #A-21202, 1:200), or a donkey anti-rat conjugated with Alexa Fluor 488 (Abcam, #ab150153, 1:200), and/or Hoechst dye (Thermo Fisher Scientific, #H3570, 1:1,000), in 1X PBS/ 0.1% Triton X-100. Coverslips were mounted on 25 × 75 x 1.0 mm

microscope glass slides, on a drop of ProLong Diamond Antifade Mountant (Thermo Fisher Scientific, #P36970).

Immunostaining on brain tissue

E18 (Fig. 7) or P0 (Fig. 5) mouse brains were fixed in 4% PFA in 1X PBS overnight at 4 °C, cryopreserved in 30% (g/vol) sucrose/0.05% sodium azide/100 mM glycine in 1X PBS, and embedded in Scigen Tissue-Plus O.C.T. Compound (Fisher Scientific, #23-730-571). 30 μm sections were obtained using a Leica CM1860 cryostat and mounted on slides. For CRE staining, slides were washed in 1X Tris-buffered saline (TBS) 3 times, 5 minutes each, and blocked for 1 h at RT in 10% donkey serum (Sigma-Aldrich Inc., #D9663)/0.3% Triton-X 100 in 1X TBS. Slides were incubated overnight with a guinea pig anti-CRE polyclonal antibody (Synaptic Systems, #257004, 1:100), a rabbit anti-DDX3X polyclonal antibody (Thermo Fisher Scientific, #A300-474A, 1:400), a rabbit anti-Fibrillarin polyclonal antibody (Abcam, #ab5821, 1:2000), a mouse monoclonal antibody raised against the 5.8S rRNA (Y10b clone, Abcam, #ab171119, 1:50), or a rat anti-CTIP2/BCL11B monoclonal antibody (Millipore, #MABE1045, 1:300) in incubation buffer (5% donkey serum/0.1% Triton-X 100 in 1X TBS). After washing, slides were incubated for 2 h at RT with a donkey anti-rabbit antibody conjugated with Alexa Fluor 647 (Thermo Fisher Scientific, #A-31573, 1:200) a donkey anti-mouse antibody conjugated with Alexa Fluor 488 (Thermo Fisher Scientific, #A-32787, 1:200), a donkey anti-guinea pig conjugated with Alexa Fluor 488 (Abcam, #ab150185, 1:200), a donkey anti-rat conjugated with Alexa Fluor 488 (Abcam, #ab150153, 1:200), and/or Hoechst dye (Thermo Fisher Scientific, #H3570, 1:1,000) in 0.1% Triton-X 100 in 1X TBS. Coverslips were mounted using Dapi-Fluoromount G (SouthernBiotech, #0100-20).

Confocal imaging

Images were acquired using a Leica TCS SP8 inverted microscope and Leica LAS X software. Excitation beams 561 and 633 nm or 405, 488, 561 or 633 nm were coupled, image size was set at 1024 ×1024 pixels, scan speed was selected at 600 Hz. 60 z-stacks of 300 nm step size (18 μm in total) were taken using a 20X air objective for dendrite analyses, and a 100X oil immersion objective for spine analyses. Z-stacks projections were prepared using the Fiji software version 2.9.0/1.53t[94]. For nucleoli and nuclei imaging, as well as imaging of rRNA, 30 z-stacks of 300 nm step size (9 μm in total) were taken using a 100X oil immersion objective with a zoom 2.

Immunofluorescence analyses

For the nucleoli analyses (Fig. 5, Fig. S6A, B), nucleoli and nuclei volumes were reconstructed from the Z-stacks images using IMARIS 10.1.0. Size for each nucleolus, sum of nucleolar volume for each nucleus, size of the nuclei, and number of nucleoli in each nucleus were measured. For the rRNA analyses (Fig. 5), the percentage of rRNA in cytoplasm or nucleus was calculated as the value raw integrated density in the cytoplasm or nucleus over the total cell using Fiji. The mean rRNA immunofluorescence signal was measured as mean of the pixel gray values on binary images using Fiji. For the DDX3X expression analyses (Fig. 1C), the fluorescence was quantified as mean of the pixel gray values, after image segmentation, using Fiji. DDX3X expression levels were measured as ratio between the mean of mCherry^{+} neurons and the average of 5 neighboring mCherry[-] within the same coverslip.

Retrograde viral tracing

5-week-old mice were anesthetized with a mixture of oxygen and isoflurane (5% induction and 1% maintenance) in an incubation chamber and placed in the stereotaxic apparatus for intracerebral injections in the reticular pontine nucleus (AP -4.00, ML 0.75, DV 4.50, based on the Allen Brain Atlas) of retrograde AAV-CAG-GFP viral particles (Addgene, #37825-AAVrg, 0.5 μl; rate of 0.1 μl/minute) using a 5 μl Hamilton microliter syringe. The needle was left in place for 5 minutes post-injection to ensure a proper diffusion of the virus into the tissue. Mice

were perfused and brains collected for posterior analysis 3 weeks after the stereotaxic injection.

Whole brain clearing and imaging

Fixed adult mouse brains with retrograde viral tracing were delipidated with a modified Adipo-Clear protocol[95,96]. Briefly, perfusion fixed brain samples were washed with B1n buffer (H2O/0.1% Triton X-100/ 0.3 M glycine, pH 7), then transferred to a methanol gradient series (20%, 40%, 60%, 80%) in B1n buffer, 4 mL for each brain, 1 h for each step; then 100% methanol for 1 h; then overnight incubation in 2:1 mixture of DCM:methanol and a 1.5 h incubation in 100% DCM the following day; then 100% methanol for 1 h three times, and reverse methanol gradient series (80%, 60%, 40%, 20%) in B1n buffer, 30 minutes for each step. Samples were then washed in B1n buffer for 1 h and overnight. The above procedures were done at RT with rocking to complete delipidation. The delipidated samples were then blocked in PTxwH buffer (PBS/0.1% Triton X100/0.05% Tween 20) with 5% DMSO and 0.3 M glycine for 3 h and overnight at 37 °C, then washed with PTxwH for 1 h, 2 h, and overnight at RT. For staining, brain samples were incubated in primary antibody (goat anti-GFP primary antibody, Rockland 600-101-215, 1:300) diluted in PTxwH for 2 weeks at 37 °C. After primary antibody incubation, samples were washed in PTxwH for 1 h, 2 h, 4 h, overnight, then 1 day, and then incubated in secondary antibody (Jackson ImmunoResearch 705-607-003, Alexa Fluor 647 donkey-anti-goat, 1:100) diluted in PTxwH at RT for 2 weeks. Samples were then washed in PTxwH for 1 h, 2 h, 4 h, overnight, and then 1 day. Samples were further fixed in 1% PFA at 4 °C overnight, washed in PTxwH at RT (1 h, 2 h, 4 h, overnight), then blocked in B1n at RT overnight, and washed in PTxwH at RT (1 h, 2 h, 4 h). Samples were then bleached in 0.3% H2O2 at 4 °C overnight, washed 3 times in 20 mM PB (16 mM Na2HPO4, 4 mM NaH2PO4 in H2O) at RT for 2 h. For further delipidation, samples were immersed in SBiP buffer four times (1 h, 2 h, 4 h, overnight, 1day X6). Next, brains were washed 2 times (2 h, 4 h) in 20 mM PB buffer and finally 2 times in PTS solution (25% 2,2′-thiodiethanol/10 mM PB) (2 h, overnight), then equilibrated with 75% histodenz buffer (Cosmo Bio USA AXS-1002424) with refractive index adjusted to 1.53 using 2,2′-thiodiethanol. Samples were stored at -20°C until acquisition. The cleared brain samples were imaged horizontally with tiling using the LifeCanvas SmartSPIM lightsheet microscope. 647 nm lasers were used for the GFP viral labeling IHC imaging with the 3.6×/0.2 detection lens. Lightsheet illumination is focused with NA 0.2 lens, and axially scanned with electrically tunable lens coupled to the camera (Hamamatsu Orca Back-Thin Fusion) in slit mode. Camera exposure was set at fast mode (2 ms) with 16b imaging. The X/Y sampling rate was 1.866 μm and Z step at 2 μm.

Sholl analysis

mCherry^{+} neurons in Fig. 1 were reconstructed using the Simple Neurite Tracer (SNT) plugin of the Fiji software in a semi-automated fashion. Dendrites were classified in primary, secondary, tertiary, and quaternary based on their outgrowth from the soma and branching patterns. The length and diameter of each dendrite were also measured. Axonal projections were excluded from the analysis. Concentric rings 10 μm apart around the somata of SNT reconstructed neurons and radiating outward were defined on SNT reconstructed neurons, and the number of intersections between the dendritic arbors and the concentric rings was counted. mCherry^{+} neurons (Fig. 6) and in vivo labeled GFP^{+} cortical neurons (Fig. 2), were analyzed as segmented images, free of axonal projections, to run an automated Sholl analysis. GFP^{+} neurons were additionally analyzed with SNT to measure the length of apical trunks and tufts.

Dendritic spine analyses

Dendritic spines were annotated on mCherry+ neurons starting at 30 μm from the soma and on 10 μm-long segments on the dendrite.

Spines were manually counted on an average of 16 10 μm-long segments per neuron, and spine count was then averaged per neuron. Dendritic spine density was measured as the total number of dendritic spines in 10 μm of dendritic length. For each spine, the head width (W) and neck length (L) was measured. Spines were classified into 6 morphological subtypes: branched (two-head spines), mushroom (W ≥ 0.7 μm; 1 < L > 3 μm), stubby (W ≤ 0.6 μm; no neck detected), thin (W ≤ 0.7 μm; L ≤ 1 μm), long thin (W ≤ 0.7 μm; 1 < L > 3 μm), and filopodia (no head detected; L ≥ 3 μm), based on previous literature[97,98].

Synaptosomes
Synaptosomes were isolated as described previously[98]. P21 *Sox2-Ddx3x+/+* and *Sox2-Ddx3x+/-* female mice were euthanized by cervical dislocation. Cortices were rapidly dissected on ice and homogenized in ice-cold homogenizing buffer (0.32 M sucrose, 1 mM EDTA, 1 mg/ml BSA, 5 mM HEPES pH=7.4) in a glass Teflon douncer, and centrifuged at $3000 \times g$ for 10 minutes at 4 °C. The supernatants were recovered and centrifuged at 14,000 g for 12 minutes at 4 °C. The pellets containing synaptosomes were gently resuspended in Krebs-Ringer buffer (140 mM NaCl, 5 mM KCl, 5 mM glucose, 1 mM EDTA, 10 mM HEPES pH 7.4), subjected to a density gradient upon addition of Percoll Plus (Sigma-Aldrich) (final 45% v/v), and centrifuged at $18,800 \times g$ for 2 minutes at 4 °C to enrich the synaptosomes at the surface of the gradient. The synaptosomes were recovered, washed in Krebs Ringer buffer, and then centrifuged at $18,800 \times g$ for 30 seconds at 4 °C. The pellets containing purified synaptosomes were lysed as detailed in the proteomics section.

Sample preparation for liquid chromatography with tandem mass spectrometry (LC-MS/MS)
Cell or synaptosome pellets were suspended in 200 μl RIPA buffer contains protease and phosphatase inhibitor cocktail. Three bursts (5% amp, 1 second pulses) of sonication for 15 seconds each were used to lyse the cells/synaptosomes. Suspension was centrifuged at 20,500 g for 10 minutes at 4 °C, and 175 μl of the supernatant was aliquoted for chloroform:methanol:water protein precipitation using standard protocols. The dried protein pellet was resuspended in 10 μl 8 M urea containing 400 mM ammonium bicarbonate (ABC), reduced with dithiothreitol (DTT), alkylated with iodoacetamide, and dual enzymatic digestion with LysC and trypsin (carried out at 37 °C overnight or 7 h, respectively). Digestion was quenched by adding trifluoroacetic acid (to 0.5%) prior to peptide de-salting with C18 MiniSpin columns (The Nest Group). The effluents from the de-salting step were dried and re-dissolved in in MS loading buffer (2% acetonitrile, 0.2% trifluoroacetic acid). Protein concentrations (A260/A280) were measured with a Nanodrop 2000 UV-Vis Spectrophotometer (Thermo Fisher Scientific). Each sample was then further diluted with MS loading buffer to 0.06 μg/μl, with 300 ng (5 μl) injected for LC-MS/MS analysis. 1:10 dilution of 10X Pierce Retention Time Calibration Mixture (Thermo Fisher Scientific, #88321) was added to each sample to check for retention time variability during LFQ data analysis.

LC-MS/MS analyses
LC-MS/MS analysis was performed on a Thermo Scientific Q Exactive HF-X equipped with a Waters M-class UPLC system utilizing a binary solvent system (A: 100% water, 0.1% formic acid; B: 100% acetonitrile, 0.1% formic acid). Trapping was performed at 10 μl/min, 99% Buffer A for 3 minutes using a Waters nanoEase M/Z Symmetry C18 Trap Column (100 Å, 5 μm, 180 μm x 20 mm). Peptides were separated using a nanoEase M/Z Peptide BEH C18 Column (130 Å, 1.7 μm, 75 μm X 250 mm) (37 °C) by elution with linear gradients reaching 6% B at 2 minutes, 25% B at 175 minutes, 40% B at 195 minutes, and 90% B at 200 minutes. Column regeneration and up to three blank injections were carried out in between all sample injections. MS was acquired in profile mode over the 350-1,500 m/z range using 1 microscan, 60,000 resolution, AGC target of 3E6, and a maximum injection time of 100 ms. Data dependent MS/MS were acquired in centroid mode on the top 20 precursors per MS scan using 1 microscan, 30,000 resolution, AGC target of 1E5, maximum injection time of 100 ms, and an isolation window of 1.6 m/z. Precursors were fragmented by HCD activation with a collision energy of 28%. MS/MS were collected on species with an intensity threshold of 2.5E4, charge states 2-6, and peptide match preferred. Dynamic exclusion was set to 20 seconds. The LC-MS/MS data were processed with Progenesis QI software (Nonlinear Dynamics, version 4.2) with protein identification carried out using in-house Mascot search engine (2.4). The Progenesis QI software performs chromatographic/spectral alignment (one run is chosen as a reference for alignment of all other data files to), mass spectral peak picking and filtering (ion signal must satisfy the 3 times standard deviation of the noise), and quantitation of proteins and peptides. A normalization factor for each run was calculated to account for differences in sample load between injections as well as differences in ionization. The normalization factor was determined by calculating a quantitative abundance ratio between the reference run and the run being normalized, with the assumption being that most proteins/peptides are not changing in the experiment so the quantitative value should equal 1. The experimental design was setup to group multiple injections (technical and biological replicates) from each run into each comparison sets. The algorithm then calculates the tabulated raw and normalized abundances, ANOVA *P*-values for each feature in the data set. The MS/MS spectra was exported as mgf (Mascot generic files) for database searching. Mascot Distiller was used to generate peak lists, and the Mascot search algorithm was used for searching against the Swiss Protein database with taxonomy restricted to *Mus musculus* (17,174 sequences); and carbamidomethyl (Cys), oxidation of Met, Phospho (Ser, Thr, Tyr), acetylation (Lys and Protein N-term), and deamidation (Asn and Asp) were entered as variable modifications. Two missed tryptic cleavages were allowed, precursor mass tolerance was set to 10 ppm, and fragment mass tolerance was set to 0.02 Da. The significance threshold was set based on a False Discovery Rate (FDR) of 2%. The Mascot search results was exported as.xml files and then imported into the processed dataset in Progenesis QI software where peptides identified were synched with the corresponding quantified features and their corresponding abundances. Protein abundances (requiring at least 1 unique peptide with MOWSE score of >95% confidence) were then calculated from the sum of all non-conflicting peptide ion ID assignment for a specific protein on each run. A label free quantitation approach utilizing Progenesis QI (Nonlinear Dynamics)[99] was utilized to obtain quantitative information on peptides and proteins. Downstream analyses were restricted to proteins identified with at least two unique peptides. The mass spectrometry proteomics data have been deposited to the ProteomeXchange Consortium via the PRIDE[100] partner repository with the dataset identifier PXD060033.

Puromycin-based assay
Details are described in the Supplemental Note.

Developmental milestones
Testing was performed as reported previously[24], using a battery of tests adapted from the Fox scale[101,102]. Details are described in the Supplemental Note.

Gait analyses
Details are described in the Supplemental Note.

Adult motor testing
Testing started at 10 weeks ± one week. Behavioral testing was conducted during the light phase in sound-attenuated rooms. Mice were handled daily for one week prior to behavioral testing to assess general health, physical appearance, and spontaneous activity (Supplemental Note). Mice were habituated to the testing room for 30 minutes prior

to testing. All surfaces and equipment were cleaned with Rescue Veterinary disinfectant between trials and nitrile gloves were used. The four genotypes were tested on the same day in randomized order by an experimenter blind to genotype. All data were scored and analyzed blind to the genotype. For accelerating rotarod, mice were tested on a motorized rod measuring 3 cm in diameter (Omnitech Electronics Inc) with gradual speed increase from 4 to 40 rpm over 5 minutes. Mice were presented with four 5 min-trials per day, 1 h apart, over three consecutive days. The latency to fall and speed was recorded. The balance beam test was conducted as described previously[24]. Briefly, the beam consisted of a 70-cm long square prism with 1.3 cm face placed horizontally 40 cm above the bench. Each frame was 5-cm long. Mice were allowed to freely walk on the beam for two sessions (one training and one testing) of 2 minutes each, separated by 4 h. The number of slips and the distance covered during the testing session were analyzed. The vertical pole test was conducted as described previously[24]. A wooden pole wrapped in tape to facilitate walking was used. The test consisted of two consecutive training days and a testing day (3 trials each day). Mice were placed facing upwards just below the top of the pole and the time to complete the turn and the time to climb down the pole were measured. The wire hanging test was conducted as described previously[24]. Mice were led from the base of the tail and allowed to grasp a rod placed 40 cm above the bench by both fore-paws. The task consisted of a 5 sec-training session followed by three 60 sec-testing sessions. The latency to fall and the distance traveled along the hanger were recorded, and the average of the testing sessions was used for analysis.

Statistical analyses

All statistics and plots were generated using the R packages stats and ggplot2. Statistical tests, number of animals in each experiment, and significance are indicated in each figure and/or corresponding legend. Data are shown as mean ± SEM, except for the plots showing empirical cumulative distribution function (ECDF). ECDF plots display data points from lowest to highest (X axis) against their percentiles (Y axis). Outliers were defined as data points below Q1-1.5xIQR or above Q3 + 1.5xIQR, where Q1 is the first quartile, Q3 is the third quartile, and the IQR is the interquartile range. Outliers, shown in plots with the ⊗ symbol, were removed from the calculations of the mean and SEM and for the statistical testing. Shapiro–Wilk test was used to assess normality and Bartlett's test to assess homoscedasticity. One-way or two-way repeated measure ANOVA was used for repeated observations. In case of multiple comparisons, one-way, two-way, or three-way ANOVA test was employed for normally distributed data with equal variance, Welch ANOVA for normally distributed data with unequal variance, or Kruskal-Wallis test for non-parametric data. Groups comparisons were then conducted with Student's t test for normally distributed data with equal variance, Welch Two Sample t test for normally distributed data with unequal variance, or Wilcoxon signed-rank test for not normally distributed data, with Benjamini-Hochberg correction for multiple comparisons. To compare empirical cumulative distribution function across groups, Kolmogorov–Smirnov test was used.

Reporting summary

Further information on research design is available in the Nature Portfolio Reporting Summary linked to this article.

Data availability

Source data are provided with this paper. The processed proteomic data generated in this study are available in Supplementary Data 1 and Supplementary Data 2. The corresponding raw proteomic data have been deposited in the ProteomeXchange under identifier PXD060033.

Further information and requests for resources and reagents should be directed to and will be fulfilled by the Lead Contact, Silvia De Rubeis (silvia.derubeis@mssm.edu). Source data are provided with this paper.

References

1. Deciphering Developmental Disorders, S. Large-scale discovery of novel genetic causes of developmental disorders. *Nature* **519**, 223–228 (2015).
2. Tang, L. et al. Prospective and detailed behavioral phenotyping in DDX3X syndrome. *Mol. Autism* **12**, 36 (2021).
3. Lennox, A. L. et al. Pathogenic DDX3X Mutations Impair RNA metabolism and neurogenesis during fetal cortical development. *Neuron* **106**, 404–420.e408 (2020).
4. Ruzzo, E. K. et al. Inherited and de novo genetic risk for autism impacts shared networks. *Cell* **178**, 850–866.e826 (2019).
5. Snijders Blok, L. et al. Mutations in DDX3X are a common cause of unexplained intellectual disability with gender-specific effects on WNT signaling. *Am. J. Hum. Genet.* **97**, 343–352 (2015).
6. Wang, X. et al. Phenotypic expansion in DDX3X - a common cause of intellectual disability in females. *Ann. Clin. Transl. Neurol.* **5**, 1277–1285 (2018).
7. Ng-Cordell, E. et al. Social and emotional characteristics of girls and young women with DDX3X-associated intellectual disability: a descriptive and comparative study. *J. Autism Dev. Disord.* **53**, 3208–3219 (2023).
8. Kellaris, G. et al. A hypomorphic inherited pathogenic variant in DDX3X causes male intellectual disability with additional neuro-developmental and neurodegenerative features. *Hum. Genomics* **12**, 11 (2018).
9. Nordahl, C. W. Why do we need sex-balanced studies of autism? *Autism Res* **16**, 1662–1669 (2023).
10. Soto-Rifo, R. et al. DEAD-box protein DDX3 associates with eIF4F to promote translation of selected mRNAs. *EMBO J.* **31**, 3745–3756 (2012).
11. Calviello, L. et al. DDX3 depletion represses translation of mRNAs with complex 5′ UTRs. *Nucleic Acids Res.* **49**, 5336–5350 (2021).
12. Hoye, M. L. et al. Aberrant cortical development is driven by impaired cell cycle and translational control in a DDX3X syndrome model. *Elife* **11**, e78203 (2022).
13. Shih, J. W. et al. Critical roles of RNA helicase DDX3 and its interactions with eIF4E/PABP1 in stress granule assembly and stress response. *Biochem J.* **441**, 119–129 (2012).
14. Fiorenzani, C., Mossa, A. & De Rubeis, S. DEAD/DEAH-box RNA helicases shape the risk of neurodevelopmental disorders. *Trends Genet* https://doi.org/10.1016/j.tig.2024.12.006 (2025).
15. Shen, H. et al. Sexually dimorphic RNA helicases DDX3X and DDX3Y differentially regulate RNA metabolism through phase separation. *Mol. Cell* **82**, 2588–2603.e2589 (2022).
16. Hondele, M. et al. DEAD-box ATPases are global regulators of phase-separated organelles. *Nature* **573**, 144–148 (2019).
17. Saito, M. et al. Acetylation of intrinsically disordered regions regulates phase separation. *Nat. Chem. Biol.* **15**, 51–61 (2019).
18. Yanas, A., Shweta, H., Owens, M. C., Liu, K. F. & Goldman, Y. E. RNA helicases DDX3X and DDX3Y form nanometer-scale RNA-protein clusters that support catalytic activity. *Curr. Biol.* **34**, 5714–5727.e5716 (2024).
19. Owens, M. C. et al. Specific catalytically impaired DDX3X mutants form sexually dimorphic hollow condensates. *Nat. Commun.* **15**, 9553 (2024).
20. Salamon, I. et al. Celf4 controls mRNA translation underlying synaptic development in the prenatal mammalian neocortex. *Nat. Commun.* **14**, 6025 (2023).
21. Harnett, D. et al. A critical period of translational control during brain development at codon resolution. *Nat. Struct. Mol. Biol.* **29**, 1277–1290 (2022).

22. Duffy, E. E. et al. Developmental dynamics of RNA translation in the human brain. *Nat. Neurosci.* **25**, 1353–1365 (2022).

23. Borisova, E. et al. Protein translation rate determines neocortical neuron fate. *Nat. Commun.* **15**, 4879 (2024).

24. Boitnott, A. et al. Developmental and behavioral phenotypes in a mouse model of DDX3X syndrome. *Biol. Psychiatry* **90**, 742–755 (2021).

25. Patmore, D. M. et al. DDX3X suppresses the susceptibility of hindbrain lineages to medulloblastoma. *Dev. Cell* **54**, 455–470 e455 (2020).

26. Chen, C. Y. et al. Targeted inactivation of murine Ddx3x: essential roles of Ddx3x in placentation and embryogenesis. *Hum. Mol. Genet* **25**, 2905–2922 (2016).

27. Chen, H. H., Yu, H. I. & Tarn, W. Y. DDX3 modulates neurite development via translationally activating an RNA regulon involved in Rac1 activation. *J. Neurosci.* **36**, 9792–9804 (2016).

28. Garieri, M. et al. Extensive cellular heterogeneity of X inactivation revealed by single-cell allele-specific expression in human fibroblasts. *Proc. Natl Acad. Sci. USA* **115**, 13015–13020 (2018).

29. Tukiainen, T. et al. Landscape of X chromosome inactivation across human tissues. *Nature* **550**, 244–248 (2017).

30. Oliva, M. et al. The impact of sex on gene expression across human tissues. *Science* **369**, eaba3066 (2020).

31. Borensztein, M. et al. Contribution of epigenetic landscapes and transcription factors to X-chromosome reactivation in the inner cell mass. *Nat. Commun.* **8**, 1297 (2017).

32. Bellott, D. W. et al. Mammalian Y chromosomes retain widely expressed dosage-sensitive regulators. *Nature* **508**, 494–499 (2014).

33. Arnold, A. P. X chromosome agents of sexual differentiation. *Nat. Rev. Endocrinol.* **18**, 574–583 (2022).

34. Cortez, D. et al. Origins and functional evolution of Y chromosomes across mammals. *Nature* **508**, 488–493 (2014).

35. Lukin, J., Smith, C. M. & De Rubeis, S. Emerging X-linked genes associated with neurodevelopmental disorders in females. *Curr. Opin. Neurobiol.* **88**, 102902 (2024).

36. Foresta, C., Ferlin, A. & Moro, E. Deletion and expression analysis of AZFa genes on the human Y chromosome revealed a major role for DBY in male infertility. *Hum. Mol. Genet.* **9**, 1161–1169 (2000).

37. Dicke, A. K. et al. DDX3Y is likely the key spermatogenic factor in the AZFa region that contributes to human non-obstructive azoospermia. *Commun. Biol.* **6**, 350 (2023).

38. Ramathal, C. et al. DDX3Y gene rescue of a Y chromosome AZFa deletion restores germ cell formation and transcriptional programs. *Sci. Rep.* **5**, 15041 (2015).

39. Vogt, P. H., Rauschendorf, M. A., Zimmer, J., Drummer, C. & Behr, R. AZFa Y gene, DDX3Y, evolved novel testis transcript variants in primates with proximal 3 UTR polyadenylation for germ cell specific translation. *Sci. Rep.* **12**, 8954 (2022).

40. Scala, M. et al. Three de novo DDX3X variants associated with distinctive brain developmental abnormalities and brain tumor in intellectually disabled females. *Eur. J. Hum. Genet* **27**, 1254–1259 (2019).

41. Ditton, H. J., Zimmer, J., Kamp, C., Rajpert-De Meyts, E. & Vogt, P. H. The AZFa gene DBY (DDX3Y) is widely transcribed but the protein is limited to the male germ cells by translation control. *Hum. Mol. Genet* **13**, 2333–2341 (2004).

42. Chauvin, C. et al. Involvement of human release factors eRF3a and eRF3b in translation termination and regulation of the termination complex formation. *Mol. Cell Biol.* **25**, 5801–5811 (2005).

43. Gong, C. et al. Sequential inverse dysregulation of the RNA helicases DDX3X and DDX3Y facilitates MYC-driven lymphomagenesis. *Mol. Cell* **81**, 4059–4075.e4011 (2021).

44. Deuel, T. A. et al. Genetic interactions between doublecortin and doublecortin-like kinase in neuronal migration and axon outgrowth. *Neuron* **49**, 41–53 (2006).

45. Sawada, M. et al. PlexinD1 signaling controls morphological changes and migration termination in newborn neurons. *EMBO J.* **37**, e97404 (2018).

46. Hor, C. H. H. & Goh, E. L. K. Rab23 regulates radial migration of projection neurons via N-cadherin. *Cereb. Cortex* **28**, 1516–1531 (2018).

47. Na, Y. et al. Fbxo45 Binds SPRY motifs in the extracellular domain of N-cadherin and regulates neuron migration during brain development. *Mol. Cell Biol.* **40**, e00539–19 (2020).

48. Karczewski, K. J. et al. The mutational constraint spectrum quantified from variation in 141,456 humans. *Nature* **581**, 434–443 (2020).

49. Thormann, A. et al. Flexible and scalable diagnostic filtering of genomic variants using G2P with Ensembl VEP. *Nat. Commun.* **10**, 2373 (2019).

50. Fu, J. M. et al. Rare coding variation provides insight into the genetic architecture and phenotypic context of autism. *Nat. Genet* **54**, 1320–1331 (2022).

51. Heyne, H. O. et al. De novo variants in neurodevelopmental disorders with epilepsy. *Nat. Genet* **50**, 1048–1053 (2018).

52. Epi, K. C., Epilepsy Phenome/Genome, P. Ultra-rare genetic variation in common epilepsies: a case-control sequencing study. *Lancet Neurol.* **16**, 135–143 (2017).

53. Epi25 Collaborative. Electronic address, s. b. u. e. a. & Epi, C. Ultra-Rare genetic variation in the epilepsies: A whole-exome sequencing study of 17,606 Individuals. *Am. J. Hum. Genet.* **105**, 267–282 (2019).

54. Mercaldo, V. et al. Altered striatal actin dynamics drives behavioral inflexibility in a mouse model of fragile X syndrome. *Neuron* **111**, 1760–1775 e1768 (2023).

55. Koopmans, F. et al. SynGO: An evidence-based, expert-curated knowledge base for the synapse. *Neuron* **103**, 217–234 e214 (2019).

56. Schmidt, E. K., Clavarino, G., Ceppi, M. & Pierre, P. SUnSET, a nonradioactive method to monitor protein synthesis. *Nat. Methods* **6**, 275–277 (2009).

57. Hoeffer, C. A. et al. Inhibition of the interactions between eukaryotic initiation factors 4E and 4G impairs long-term associative memory consolidation but not reconsolidation. *Proc. Natl Acad. Sci. USA* **108**, 3383–3388 (2011).

58. Fusco, C. M. et al. Neuronal ribosomes exhibit dynamic and context-dependent exchange of ribosomal proteins. *Nat. Commun.* **12**, 6127 (2021).

59. Seo, S. S. et al. Excess ribosomal protein production unbalances translation in a model of Fragile X Syndrome. *Nat. Commun.* **13**, 3236 (2022).

60. Scarnati, M. S., Kataria, R., Biswas, M. & Paradiso, K. G. Active presynaptic ribosomes in the mammalian brain, and altered transmitter release after protein synthesis inhibition. *Elife* **7**, e36697 (2018).

61. Akbalik, G. et al. Visualization of newly synthesized neuronal RNA in vitro and in vivo using click-chemistry. *RNA Biol.* **14**, 20–28 (2017).

62. Chau, K. F. et al. Downregulation of ribosome biogenesis during early forebrain development. *Elife* **7**, e36998 (2018).

63. Salehi, S. et al. Cytosolic Ptbp2 modulates axon growth in motoneurons through axonal localization and translation of Hnrnpr. *Nat. Commun.* **14**, 4158 (2023).

64. Kondrashov, N. et al. Ribosome-mediated specificity in Hox mRNA translation and vertebrate tissue patterning. *Cell* **145**, 383–397 (2011).

65. Metz, J. B. et al. High-throughput translational profiling with riboPLATE-seq. *Sci. Rep.* **12**, 5718 (2022).

66. Calvino, F. R. et al. Symportin 1 chaperones 5S RNP assembly during ribosome biogenesis by occupying an essential rRNA-binding site. *Nat. Commun.* **6**, 6510 (2015).

67. Leidig, C. et al. 60S ribosome biogenesis requires rotation of the 5S ribonucleoprotein particle. *Nat. Commun.* **5**, 3491 (2014).

68. Mensah, M. A. et al. Aberrant phase separation and nucleolar dysfunction in rare genetic diseases. *Nature* **614**, 564–571 (2023).

69. Valentin-Vega, Y. A. et al. Cancer-associated DDX3X mutations drive stress granule assembly and impair global translation. *Sci. Rep.* **6**, 25996 (2016).

70. Toyama, Y. & Shimada, I. NMR characterization of RNA binding property of the DEAD-box RNA helicase DDX3X and its implications for helicase activity. *Nat. Commun.* **15**, 3303 (2024).

71. Xiol, J. et al. RNA clamping by Vasa assembles a piRNA amplifier complex on transposon transcripts. *Cell* **157**, 1698–1711 (2014).

72. Kast, R. J., Lanjewar, A. L., Smith, C. D. & Levitt, P. FOXP2 exhibits projection neuron class specific expression, but is not required for multiple aspects of cortical histogenesis. *Elife* **8**, e42012 (2019).

73. Gorski, J. A. et al. Cortical excitatory neurons and glia, but not GABAergic neurons, are produced in the Emx1-expressing lineage. *J. Neurosci.* **22**, 6309–6314 (2002).

74. Levy, T. et al. DDX3X Syndrome: Summary of Findings and Recommendations for Evaluation and Care. *Pediatr. Neurol.* **138**, 87–94 (2023).

75. Rengarajan, S., Derks, J., Bellott, D. W., Slavov, N. & Page, D. C. Post-transcriptional cross- and auto-regulation buffer expression of the human RNA helicases *DDX3X* and *DDX3Y*. https://pubmed.ncbi.nlm.nih.gov/39794123/ (2024).

76. Sidhaye, J. et al. Integrated transcriptome and proteome analysis reveals posttranscriptional regulation of ribosomal genes in human brain organoids. *Elife* **12**, e85135 (2023).

77. Anadolu, M. N. et al. Puromycin reveals a distinct conformation of neuronal ribosomes. *Proc. Natl Acad. Sci. USA* **121**, e2306993121 (2024).

78. Kraushar, M. L. et al. Protein synthesis in the developing neocortex at near-atomic resolution reveals Ebp1-mediated neuronal proteostasis at the 60S tunnel exit. *Mol. Cell* **81**, 304–322.e316 (2021).

79. De Rubeis, S. et al. Synaptic, transcriptional and chromatin genes disrupted in autism. *Nature* **515**, 209–215 (2014).

80. Clement, J. P. et al. Pathogenic SYNGAP1 mutations impair cognitive development by disrupting maturation of dendritic spine synapses. *Cell* **151**, 709–723 (2012).

81. Cruz-Martin, A., Crespo, M. & Portera-Cailliau, C. Delayed stabilization of dendritic spines in fragile X mice. *J. Neurosci.* **30**, 7793–7803 (2010).

82. Fazel Darbandi, S. et al. Enhancing WNT signaling restores cortical neuronal spine maturation and synaptogenesis in Tbr1 Mutants. *Cell Rep.* **31**, 107495 (2020).

83. Spratt, P. W. E. et al. The autism-associated gene Scn2a contributes to dendritic excitability and synaptic function in the prefrontal cortex. *Neuron* **103**, 673–685.e675 (2019).

84. Holtmaat, A. & Svoboda, K. Experience-dependent structural synaptic plasticity in the mammalian brain. *Nat. Rev. Neurosci.* **10**, 647–658 (2009).

85. Richards, S. E. V. et al. Experience-dependent development of dendritic arbors in mouse visual cortex. *J. Neurosci.* **40**, 6536–6556 (2020).

86. Jan, Y. N. & Jan, L. Y. Branching out: mechanisms of dendritic arborization. *Nat. Rev. Neurosci.* **11**, 316–328 (2010).

87. Creson, T. K. et al. Re-expression of SynGAP protein in adulthood improves translatable measures of brain function and behavior. *Elife* **8**, e46752 (2019).

88. Robinson, L. et al. Morphological and functional reversal of phenotypes in a mouse model of rett syndrome. *Brain* **135**, 2699–2710 (2012).

89. Sztainberg, Y. et al. Reversal of phenotypes in MECP2 duplication mice using genetic rescue or antisense oligonucleotides. *Nature* **528**, 123–126 (2015).

90. Garg, S. K. et al. Systemic delivery of MeCP2 rescues behavioral and cellular deficits in female mouse models of Rett syndrome. *J. Neurosci.* **33**, 13612–13620 (2013).

91. Mei, Y. et al. Adult restoration of Shank3 expression rescues selective autistic-like phenotypes. *Nature* **530**, 481–484 (2016).

92. Hayashi, S., Lewis, P., Pevny, L. & McMahon, A. P. Efficient gene modulation in mouse epiblast using a Sox2Cre transgenic mouse strain. *Mech. Dev.* **119**, S97–S101 (2002).

93. Kaech, S. & Banker, G. Culturing hippocampal neurons. *Nat. Protoc.* **1**, 2406–2415 (2006).

94. Schindelin, J. et al. Fiji: an open-source platform for biological-image analysis. *Nat. Methods* **9**, 676–682 (2012).

95. Chi, J., Crane, A., Wu, Z. & Cohen, P. Adipo-Clear: A tissue clearing method for three-dimensional imaging of adipose tissue. *J. Vis. Exp.*, https://doi.org/10.3791/58271 (2018).

96. Hou, Y. et al. Topographical organization of mammillary neurogenesis and efferent projections in the mouse brain. *Cell Rep.* **34**, 108712 (2021).

97. Risher, W. C., Ustunkaya, T., Singh Alvarado, J. & Eroglu, C. Rapid golgi analysis method for efficient and unbiased classification of dendritic spines. *PLoS One* **9**, e107591 (2014).

98. De Rubeis, S. et al. CYFIP1 coordinates mRNA translation and cytoskeleton remodeling to ensure proper dendritic spine formation. *Neuron* **79**, 1169–1182 (2013).

99. Vidyadhara, D. J. et al. Dopamine transporter and synaptic vesicle sorting defects underlie auxilin-associated parkinson's disease. *Cell Rep.* **42**, 112231 (2023).

100. Perez-Riverol, Y. et al. The PRIDE database at 20 years: 2025 update. *Nucleic Acids Res.* **53**, D543–D553 (2025).

101. Fox, W. M. Reflex-ontogeny and behavioural development of the mouse. *Anim. Behav.* **13**, 234–241 (1965).

102. Heyser, C. J. Assessment of developmental milestones in rodents. *Curr. Protoc. Neurosci.* **Chapter 8**, Unit 8 18, https://doi.org/10.1002/0471142301.ns0818s25 (2004).

103. Hempstead, E. https://BioRender.com/ndyh7n2 (2025).

104. Hempstead, E. https://BioRender.com/97593al (2025).

Acknowledgements

Author contributions

S.D.R., A.M., L.D., and J.L. conceptualize the study and designed the experiments. A.M., L.D., J.L., Y.P., C.F., Z.A., and M.G.F. conducted experiments and collected data. Z.W. and W.W. designed the whole-mount experiments and collected data. F.M., J.K., and J.T. provided input on biochemical experiments. S.D.R., A.M., L.D., and J.L. analyzed the data. S.D.R., A.M., L.D., and J.L. wrote the original draft and all the other authors edited and approved the manuscript.

Competing interests

The authors declare no competing interests.

Additional information

Supplementary information The online version contains supplementary material available at https://doi.org/10.1038/s41467-025-59680-8.

Correspondence and requests for materials should be addressed to Silvia De Rubeis.

Peer review information *Nature Communications* thanks the anonymous reviewers for their contribution to the peer review of this work. A peer review file is available.

Reprints and permissions information is available at http://www.nature.com/reprints

Publisher's note Springer Nature remains neutral with regard to jurisdictional claims in published maps and institutional affiliations.